Coordination Chemistry Reviews 253 (2009) 2116–2130

Contents lists available at ScienceDirect

Coordination Chemistry Reviews

journal homepage: www.elsevier.com/locate/ccr

Review

The power of electron paramagnetic resonance to study asymmetric homogeneous catalysts based on transition-metal complexes

S. Van Doorslaer[a,*], I. Caretti[a], I.A. Fallis[b], D.M. Murphy[b]

[a] Department of Physics, University of Antwerp, Universiteitsplein 1, B-2610 Wilrijk-Antwerp, Belgium
[b] School of Chemistry, Cardiff University, Main Building, Park Place, Cardiff CF10 3AT, UK

Contents

ARTICLE INFO

Article history:
Received 5 November 2008
Accepted 11 December 2008
Available online 24 December 2008

Keywords:
Electron paramagnetic resonance spectroscopy
Electron spin-echo envelope modulation spectroscopy
Electron nuclear double resonance spectroscopy
Asymmetric catalysis

ABSTRACT

Asymmetric synthesis involves the preparation of chiral compounds with well-defined three-dimensional molecular structure or stereochemistry. Many of these enantioselective transformations involve chiral ligands incorporating transition-metal ions. Over the years numerous synthetic, spectroscopic and theoretical approaches have been applied to understand and probe the inner workings and mode of chiral transfer in these homogeneous based catalysts. For the paramagnetic based asymmetric complexes, electron paramagnetic resonance (EPR) can provide a wealth of detail and information on the structure and mechanism of the catalysts. Despite this potential, the application and uptake of advanced EPR methodologies to this field of endeavor has been limited. The purpose of this review is to explain and illustrate, through representative examples, the enormous amount of information that can be obtained from an EPR study of the chiral metal-based complexes, ranging from electronic structure and symmetry to spatial arrangement of interacting ligands and substrates.

* Corresponding author. Tel.: +32 3 820 24 61; fax: +32 3 820 24 70.
E-mail address: sabine.vandoorslaer@ua.ac.be (S. Van Doorslaer).

0010-8545/$ – see front matter © 2008 Elsevier B.V. All rights reserved.
doi:10.1016/j.ccr.2008.12.010

1. Introduction

In 2001 the Nobel Prize in Chemistry was awarded to Knowles, Noyori and Sharpless for their pioneering work in catalytic asymmetric synthesis; specifically on chiral, catalyzed hydrogenation and oxidation reactions. The development of chiral ligands that easily coordinate metal ions, and ultimately induce high stereoselectivities for organic transformation, therefore represents an extremely important area of modern chemistry [1]. The chiral products formed in these types of reactions are increasingly important for different industrial applications, particularly pharmaceutical and agrochemical products [2]. This importance is most obviously appreciated within the context of drug–receptor interactions, since most biological targets are chiral entities [3]. The performance of these homogeneous asymmetric catalysts, and to some extent the asymmetric heterogeneous (or supported) catalysts, will be controlled by a multitude of molecular characteristics, such as symmetry and steric properties of the catalyst and the reacting ligands, the electronic nature of the catalyst and its H-bonding capacity [4,5]. Obviously, a targeted design of optimally performing enantioselective catalysts can only be achieved through a clear understanding of the electronic and structural properties that govern the inner workings of such a catalyst. Several approaches, including theoretical density functional theory (DFT) computation and many spectroscopic analyses, have been applied to gain a greater insight into these properties and, specifically, to learn how the steric properties of the ligand contribute to the asymmetric chiral induction mechanism [6–11]. A particularly challenging problem remains the experimental detection of weak inner and outer sphere substrate–ligand interactions that determine the mode of chiral information transfer between substrate and ligand [12].

Paramagnetic transition-metal ions form the core of many important homogeneous (asymmetric) catalysts. Although electron paramagnetic resonance (EPR) offers an excellent tool to analyze paramagnetic materials, its potential is largely unexploited and indeed underestimated in the field of homogeneous catalysis. The majority of the EPR studies applied to the fields of homogeneous and heterogeneous catalysis still involve continuous-wave (CW)-EPR [13] at the conventional X-band microwave frequencies (~9.5 GHz). This contradicts the rapid changes that the field of EPR has undergone since the late 1980s, whereby many advanced pulsed and/or high-field EPR methods have been introduced that enormously increased the performance and applicability of EPR to unravel complex problems in physics, chemistry and biology [14–24].

This review aims to highlight the potential of different EPR techniques in the study of inorganic complexes and homogeneous catalysis in general, and in chiral homogeneous catalysis in particular. After a brief overview of the current state-of-the-art EPR methods, the power of these methods will be illustrated using a selected number of examples from synthetic and biological (enzymatic) catalysis. Note that this review is not meant to be exhaustive, but aims at giving a concise overview of the usefulness of advanced multi-frequency-EPR techniques. More exhaustive reviews on the EPR methodology or on the general applications of EPR can be found in the literature [14–24].

2. The EPR method in a nutshell

2.1. CW-EPR

As already mentioned in the introduction, the majority of all EPR studies are still carried out using X-band continuous-wave (CW) EPR. CW-EPR relies on the electron Zeeman effect: when a paramagnetic compound is placed in an external magnetic field, B_0, the energy of the different spin states will depend linearly on B_0 and on the magnetic quantum number, m_S [13]. For the simple case of one unpaired electron ($S = 1/2$, $m_S = \pm 1/2$), the magnetic field will split the originally degenerate energy levels in two (Fig. 1). The state of the electron spin (determined by its m_S value) can be changed by irradiation with microwaves, provided the frequency matches the resonance condition:

$$h\nu_{mw} = g\beta_e B_0, \quad (1)$$

where β_e is the Bohr magneton, h is Planck's constant and ν_{mw} is the microwave frequency. The g factor is characteristic of the local environment around the electron and the value depends on the orientation of the molecule with respect to the magnetic field. This orientation dependence, which is nothing other than a reflection of the symmetry and anisotropy of the local surroundings, is expressed mathematically by the so-called $\boldsymbol{g}$ tensor. The $\boldsymbol{g}$ tensor is fully characterized by its three principal g values (g_x, g_y and g_z) and by the orientation of the corresponding principal $\boldsymbol{g}$ axes in the molecular frame [13].

In an X-band CW-EPR experiment, the microwave frequency is chosen in the X-band, *i.e.* around 9.5 GHz. This frequency is kept fixed while the absorption of microwaves is monitored as a function of the varying external magnetic field. When the resonance condition (1) is fulfilled, absorption of microwaves will be detected. For technical reasons, the first derivative of this absorption signal is normally detected. In the case of single crystals, the $\boldsymbol{g}$ tensor and its principal directions can be fully determined through CW-EPR measurements at different crystal orientations in the magnetic field (so-called angular variations). However, in the case of disordered

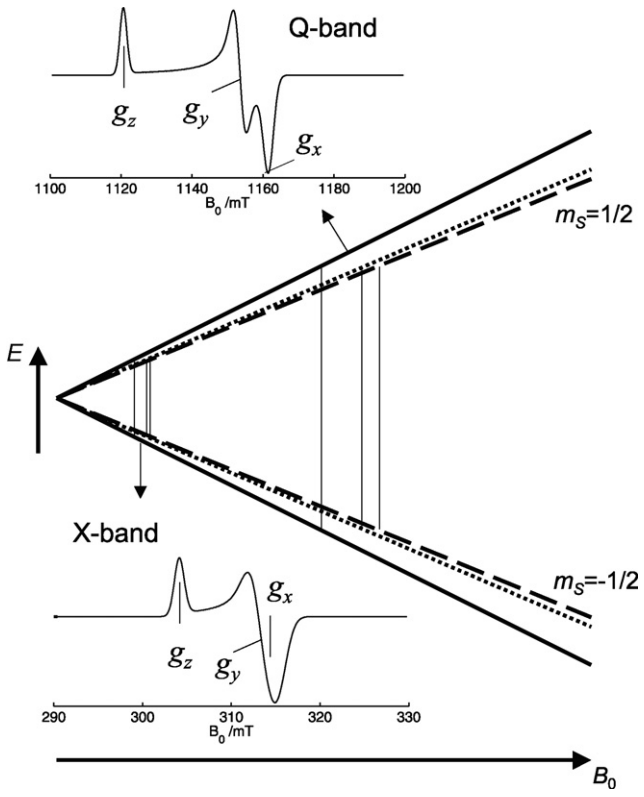

Fig. 1. Schematic illustration showing the lifting of the degeneracy of the m_S manifolds by an increasing external magnetic field B_0 (electron Zeeman effect). The three pairs of lines correspond to the situations found for $\boldsymbol{B}_0$ parallel to the $\boldsymbol{g}_z$ axis (solid lines), $\boldsymbol{g}_y$ axis (dotted lines) and $\boldsymbol{g}_x$ axis (dashed lines) of an $S = 1/2$ system characterized by $g_x = 2.1527$, $g_y = 2.1678$ and $g_z = 2.2312$. The corresponding powder-like CW-EPR spectra for this system are simulated at Q-band (35 GHz) and X-band (9.5 GHz) mw frequencies. In relation with the energy scheme, this illustrates the resolution enhancement achieved at higher mw frequencies.

systems, like frozen solutions of metal complexes or enzymes, the CW-EPR spectrum will be the sum of all spectra belonging to all possible orientations of the molecule in the magnetic field. This leads to so-called powder-type spectra, a typical example of which is depicted in Fig. 1. In powder spectra, the principal g values can be obtained through spectral simulations, but all information about the orientation of the $\boldsymbol{g}$ tensor in the molecular frame is lost.

Although X-band CW-EPR has many advantages, there are also many drawbacks when only this technique is used. If the principal g values differ only slightly, this difference may not be resolved in the X-band CW-EPR spectra. Furthermore, in order to perform X-band EPR, one needs a significant amount of sample (typical sample volume is 0.1–0.2 cm^3), which is not always available, especially for biological materials. Finally, for the more complex 'high-spin' systems ($S > 1/2$), the X-band microwave quantum may be too small to induce a transition between the m_S and $m_S + 1$ level [17]. This can be circumvented using higher microwave frequencies: 35 GHz (Q-band), 95 GHz (W-band), and higher [17,19]. Fig. 1 illustrates schematically how CW-EPR spectroscopy performed at higher microwave frequencies allows for a better spectral resolution. Furthermore, the sample volumes needed for high-field EPR are smaller. At W-band the volumes are typically a factor 100 times smaller than needed for X-band EPR. This relates to the 10-fold smaller wavelength of the microwaves (W-band: $\lambda_{mw} \sim 3$ mm; X-band: $\lambda_{mw} \sim 3$ cm).

The situation described by Eq. (1) holds only for a system with one unpaired electron ($S = 1/2$), which is surrounded by non-magnetic nuclei. This is, however, very rare. In most systems, the unpaired electron(s) are surrounded by many magnetic nuclei with a nuclear spin I. For the metal complexes reviewed here, these nuclei range from ligand- and substrate-based nuclei, such as ^{1}H ($I = 1/2$), ^{14}N ($I = 1$), ^{13}C ($I = 1/2$), ^{31}P ($I = 1/2$), to the central metal ions themselves, such as ^{59}Co ($I = 7/2$), ^{63,65}Cu ($I = 3/2$), ^{51}V ($I = 7/2$), *etc*. The spin system is then described using the spin Hamiltonian [13]:

$$\hat{H} = \frac{\beta_e \tilde{\boldsymbol{B}}_0 \boldsymbol{g} \boldsymbol{S}}{h} + \tilde{\boldsymbol{S}} \boldsymbol{D} \boldsymbol{S} + \sum_k \left(\tilde{\boldsymbol{S}} \boldsymbol{A}_k \boldsymbol{I}_k - \frac{\beta_n g_{n,k} \tilde{\boldsymbol{B}}_0 \boldsymbol{I}_k}{h} \right) + \sum_{k, I_k > 1/2} \tilde{\boldsymbol{I}}_k \boldsymbol{P}_k \boldsymbol{I}_k, \quad (2)$$

where β_n is the nuclear magneton, $g_{n,k}$ is the nuclear g factor, $\boldsymbol{A}_k$ is the hyperfine tensor, $\boldsymbol{D}$ is the zero-field tensor and $\boldsymbol{P}_k$ is the nuclear-quadrupole tensor. The first term of the spin Hamiltonian is the electron Zeeman interaction explained earlier. The second term, so-called zero-field splitting (zfs) term, is only present for $S > 1/2$ systems and reflects the dipole–dipole coupling between the electron spins and the spin–orbit contributions. The latter contribution is usually dominating for transition-metal ions. The third term is the hyperfine interaction between the unpaired electron and the surrounding magnetic nuclei. The fourth term is the nuclear Zeeman interaction, whereby $g_{n,k}$ identifies the type of interacting nucleus. The last term is only important if the magnetic nuclei have a nuclear spin larger than 1/2. It represents the nuclear-quadrupole interaction, which stems from the interaction of the non-spherical charge distribution of the nucleus with the electric field gradient, caused by the electrons and nuclei in the environment of the nucleus.

Within the context of the examples covered in this review, it is important to focus more on the hyperfine interaction [13]. As discussed for the $\boldsymbol{g}$ tensor, the hyperfine interaction also depends on the orientation of the magnetic field with respect to the molecular axes ($\boldsymbol{A}$ is a 3×3 matrix characterized by its principal values A_x, A_y and A_z, and the corresponding principal axes). The hyperfine tensor is the sum of an isotropic (Fermi contact) term stemming from the finite probability of the unpaired electron to be at the nucleus, and a dipole-dipole contribution (represented by $\boldsymbol{T}$). In the case where the distance, r, between the electron and the nucleus is larger than 0.26 nm and the spin delocalization is small, the latter contribution can be written as:

$$T_{ij} = \frac{\mu_0}{4\pi} \frac{1}{r^3} g_n \beta_n \beta_e g_i (3 r_i r_j - \delta_{ij}) \quad (i, j = x, y, z), \quad (3)$$

where r_x, r_y, and r_z are the direction cosines of the electron–nucleus vector in the $\boldsymbol{g}$ tensor axes frame. For all other cases, the anisotropic part of the hyperfine tensor will also contain information about the types of molecular bonds that are formed (σ-bond, π-bond, *etc.*). The full set of hyperfine interactions can thus give crucial information about the spin-density distribution and electronic structure of the sample, and can reveal the local geometry of the paramagnetic site. In the case of transition-metal ions, for instance, the transition-metal hyperfine tensor and the corresponding $\boldsymbol{g}$ tensor lead to a direct identification of the ion, its oxidation state, its ground-state and the local symmetry [25]. As we will demonstrate later, this information is vitally important in the derivation of any model concerning structure–function relations in asymmetric catalysts, which incorporate paramagnetic transition-metal ions.

In order to observe the hyperfine interactions, one needs to combine different EPR techniques. The strongest central metal hyperfine couplings may well be resolved in a CW-EPR experiment. This is illustrated for example in Fig. 2a, depicting the X-band CW-EPR spectrum of a VO^{II} complex in a frozen solution (resulting in a powder-type EPR pattern). In this case, the interaction with the ^{51}V

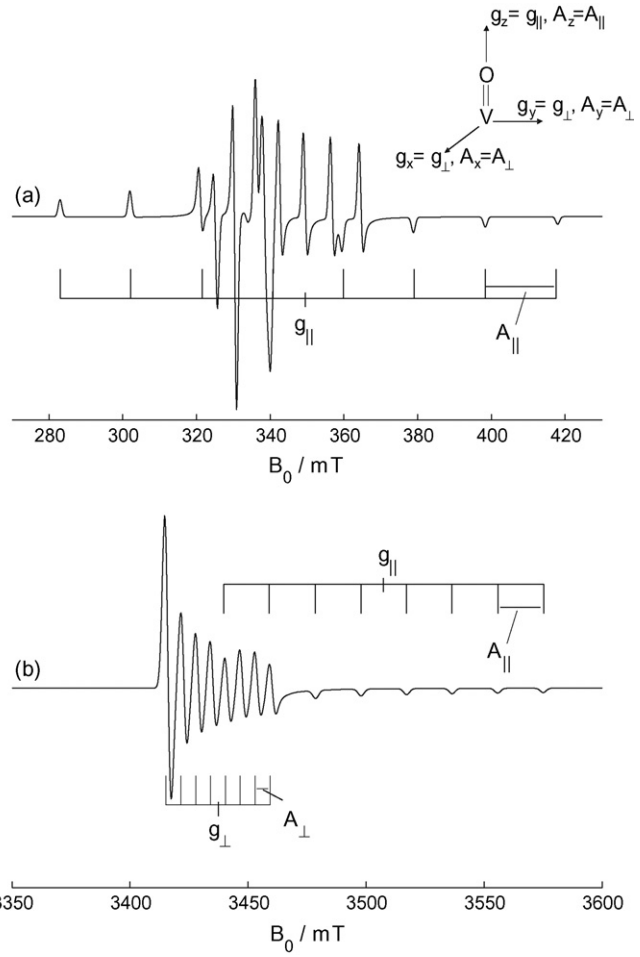

Fig. 2. Simulated X-band (a) and W-band (b) CW-EPR spectrum of a typical square-pyramidal VO^{II} complex using the following simulation parameters: $g_z = g_{||} = 1.935$, $g_{x,y} = g_{\perp} = 1.974$, $A_z = A_{||} = 522$ MHz and $A_{x,y} = A_{\perp} = 170$ MHz. The schematic illustration in the upper right corner shows the orientation of the principal $\boldsymbol{g}$ axes versus the VO^{II} unit. The principal g and hyperfine values can easily be read off from the W-band CW-EPR spectrum (b), where the $g_{\perp}$ and $A_{\perp}$ features in the centre of the X-band CW-EPR spectrum (a) are difficult to interpret without simulations.

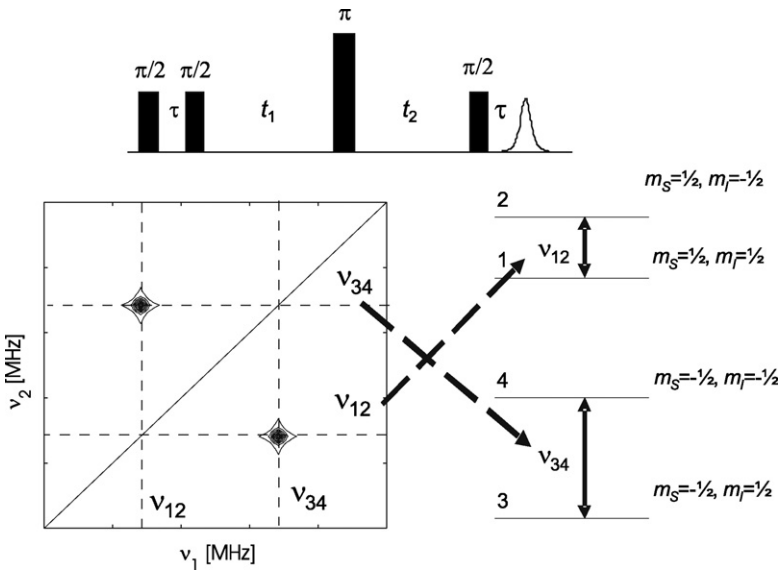

Fig. 3. Top: HYSCORE pulse sequence. Bottom left: Schematic representation of a single-crystal HYSCORE spectrum based on a simple $S = 1/2$, $I = 1/2$ spin system, with positive g_n and hyperfine coupling. The hyperfine coupling is smaller than twice the Zeeman interaction (weak coupling case). Bottom right: energy level scheme corresponding to this $S = 1/2$, $I = 1/2$ system. ν_{12} and ν_{34} are the nuclear frequencies corresponding to the $|\Delta m_S| = 0$, $|\Delta m_I| = 1$ transitions.

($I = 7/2$) nucleus leads to an additional splitting of each EPR line into eight lines. It will be obvious to the reader that this additional structure significantly complicates the profile and hence interpretation of the spectrum. Fig. 2b shows the corresponding W-band CW-EPR spectrum. At higher frequencies, the signal has become significantly simpler, and the principal g and hyperfine values can be measured directly from the spectrum. Indeed, the higher field has separated the $g_z = g_{||}$ from the $g_{x,y} = g_\perp$ region, so that the corresponding 8-line patterns no longer overlap. This simple example illustrates one of the strengths of high-field EPR.

Unlike the central metal hyperfine couplings, in most cases, the ligand hyperfine interactions cannot be resolved in a CW-EPR experiment, because, for an electron interacting with n nuclear spins I_n, each EPR line splits into $\prod_n(2I_n + 1)$ lines, which quickly leads to broad lines lacking all substructure. In order to observe the different ligand hyperfine interactions that give important information about the homogeneous catalysts, more advanced methods need to be applied. These methods can be divided into three groups: ESEEM (electron–spin-echo envelope modulation)-type experiments, ENDOR (electron–nuclear double resonance)-type experiments and ELDOR (electron–electron double resonance)-detected NMR experiments. These experiments will allow for a detection of the nuclear frequencies that contain the information of the hyperfine interactions, nuclear-quadrupole couplings (for $I_n > 1/2$) and the nuclear Zeeman interactions. A short overview of these techniques is given in Sections 2.2–2.4.

2.2. ESEEM-type experiments

ESEEM techniques are very well suited for the detection of small nuclear frequencies (<20 MHz). In the region below 5 MHz, their performance is superior to the ENDOR and ELDOR-detected NMR techniques discussed in the next sections. In the ESEEM experiment, the sample is no longer continuously irradiated with microwaves. By analogy to the well-known pulsed NMR experiments [26], the electron magnetization is now manipulated with microwave pulses. In ESEEM, a sequence of microwave pulses is applied that generates an electron spin echo (ESE). The echo intensity is monitored as a function of a variation in one or more pulse intervals. This leads to a one- or multi-dimensional time-domain signal. When the pulse sequence and varying time intervals are adequately chosen, the echo intensity will be modulated with the nuclear frequencies. The physical background of this modulation effect is described in detail in reference [20] and will not be explained in this text. Subsequent Fourier transformation of the time traces allows for a direct determination of the nuclear frequencies.

Although different ESEEM experiments are widely used [20], we will draw particular attention to the two-dimensional HYSCORE (hyperfine sublevel correlation) spectroscopy [27] (Fig. 3). An analogy can be drawn with the many correlation techniques used in NMR, such as COSY. In correlation-type experiments, the introduction of a well chosen mixing pulse sequence between two variable evolution periods induces specific cross peaks correlating the nuclear frequencies according to their specific characteristics (for instance, correlation of the frequencies of spin–spin-coupled nuclei in COSY) [26]. In the four-pulse HYSCORE experiment, the mixing π pulse between the two evolution times, t_1 and t_2, leads to a correlation between the nuclear frequencies of two different m_S manifolds. These cross peaks can be immediately interpreted in terms of the individual nuclear contributions as illustrated in Fig. 3 for a simple case of one unpaired electron ($S = 1/2$) interacting with a nuclear spin $I = 1/2$ (e.g. a proton). The HYSCORE cross peaks facilitate the analysis of complex ESEEM spectra.

In the last decade, the performance of the HYSCORE technique has been improved by the introduction of matched HYSCORE [28] and SMART HYSCORE [29]. The technique is by now one of the major pulsed EPR methods used to detect nuclear frequencies. Once again, for more specific details, we refer the reader to the specialized literature [20].

2.3. ENDOR-type experiments

In the different ENDOR-type experiments, a combination of radiofrequency (rf) waves and microwaves are used to obtain information about the nuclear frequencies. Both CW and pulsed versions of the ENDOR technique are known and widely used. CW-ENDOR was introduced in 1956 by Feher [30]. The basics behind this experiment are simple [30,31]. At a given magnetic field setting, the CW-EPR signal (e.g. EPR transition 2–4 in the energy level scheme in Fig. 3) is saturated by increasing the microwave power. The recovery

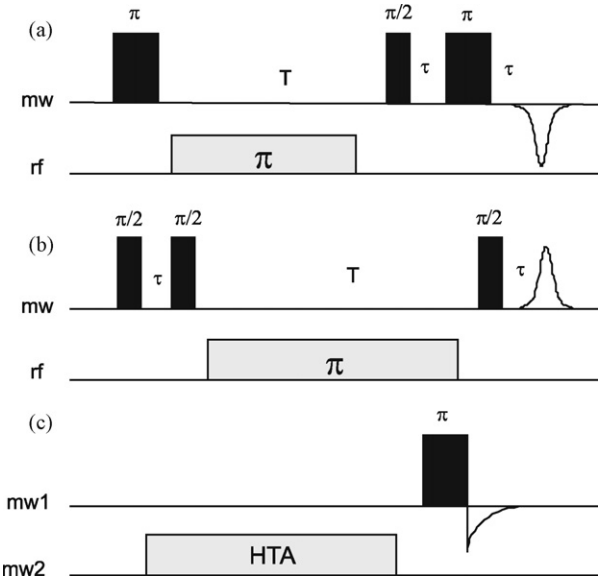

Fig. 4. Pulsed ENDOR and ELDOR-detected NMR sequences. mw = microwave; rf = radio frequency. (a) Davies-ENDOR (in the experiment, the rf frequency is swept), (b) Mims-ENDOR (in this experiment the rf frequency is swept. Time τ in both sequences can be varied in a second dimension), and (c) ELDOR-detected NMR experiment with FID detection (the microwave frequency, mw2, of the high-turning angle (HTA) pulse is swept around the fixed mw1 frequency).

of this signal is detected as a function of the frequency of continuously irradiated radio waves. When the radio frequency matches one of the nuclear frequencies, the populations of all energy levels will be changed and a net microwave absorption (*i.e.* an EPR signal) can again be detected. In our example, the 2–4 transition will be desaturated when the rf frequency equals ν_{12} or ν_{34}. The CW-ENDOR signals will thus directly reflect the nuclear frequencies.

One of the drawbacks of the CW-ENDOR experiment, besides the inherent one-dimensionality of the experiment, is the fact that the electron and nuclear relaxation times usually limit the applicability of CW-ENDOR to a small temperature window. This is circumvented by pulsed ENDOR experiments [32,33], where the pulse sequence can be made short enough to avoid these relaxation effects. In pulsed ENDOR experiments, pulse sequences consisting of combinations of microwave and rf pulses are used. The two standard pulsed ENDOR experiments are Davies-ENDOR (Fig. 4a) [34] and Mims-ENDOR (Fig. 4b) [35]. In both cases, an ESE is created through the microwave pulse sequence and the effect on the echo intensity of varying the rf frequency is monitored. Mims-ENDOR is an excellent method to detect weakly coupled nuclei, *i.e.* nuclei for which the hyperfine coupling is smaller than twice the nuclear Zeeman interaction. On the other hand, Davies-ENDOR allows the detection of contributions from the stronger coupled nuclei. The pulsed ENDOR approach allows for more versatile experiments than the CW-ENDOR technique. Two-dimensional experiments, involving a combination of the radiofrequency sweep and a variation of an interpulse distance, have been developed to correlate the nuclear frequencies with specific parameters, such as the hyperfine value [20,36]. Furthermore, variation of the strength of the microwave pulses used in the pulsed ENDOR schemes can suppress selectively certain interactions (hyperfine contrast selective ENDOR) [37].

From the above explanation, it will come as no surprise that ENDOR techniques are often used to detect the different hyperfine couplings. It should be stressed, however, that for nuclear frequencies below 5 MHz, the performance of these ENDOR methods is not good and ESEEM techniques should be applied.

2.4. ELDOR-detected NMR

A last set of techniques that leads to the detection of nuclear frequencies is the so-called ELDOR-detected NMR experiments [38]. In these experiments, microwave pulses with different microwave frequency are used. Fig. 4c shows one of the basic ELDOR-detected NMR experiments. The idea behind ELDOR-detected NMR is similar to the one behind pulsed ENDOR. However, instead of using an rf pulse with variable frequency to affect directly the nuclear transitions ($|\Delta m_S| = 0$, $|\Delta m_I| = 1$) and hence influence the population difference in the electronic transition that is detected ($|\Delta m_S| = 1$, $|\Delta m_I| = 0, 1$), an additional mw pulse with a variable microwave frequency mw2 is applied. Whenever mw2 hits an electronic transition, the population of the observed electronic transition will also change. The difference between two electronic transitions is related to the nuclear frequency (see for instance the energy scheme in Fig. 3, where the difference between the two electronic transitions ν_{24} and ν_{23} equals the nuclear frequency ν_{34}). By plotting the detected signal as a function of the difference between mw2 and mw1, the nuclear frequencies can again be determined.

Although ELDOR-detected NMR experiments are far less established than ENDOR and ESEEM experiments, they complement nicely the latter techniques. At higher microwaves, ELDOR-detected NMR techniques perform better than Davies-ENDOR for the detection of strongly coupled high-spin nuclei [39]. Recently, a combined ELDOR-detected NMR/ENDOR experiment has been introduced, referred to as triple hyperfine sublevel correlation experiment (THYCOS) [40] that further expands the potential of these methods.

2.5. The multi-frequency approach

In Fig. 2 we already illustrated that performing high-field CW-EPR not only facilitates the evaluation of the principal g values, but may also allow for a more facile analysis of the hyperfine contributions visible in the CW-EPR spectra. The multi-frequency approach is, however, even more important in ESEEM, ENDOR and ELDOR-detected NMR experiments. Since the nuclear Zeeman interaction linearly depends on the magnetic field, the nuclear spectra of different magnetic nuclei will be separated more at higher magnetic fields. This is demonstrated in Fig. 5, showing the difference

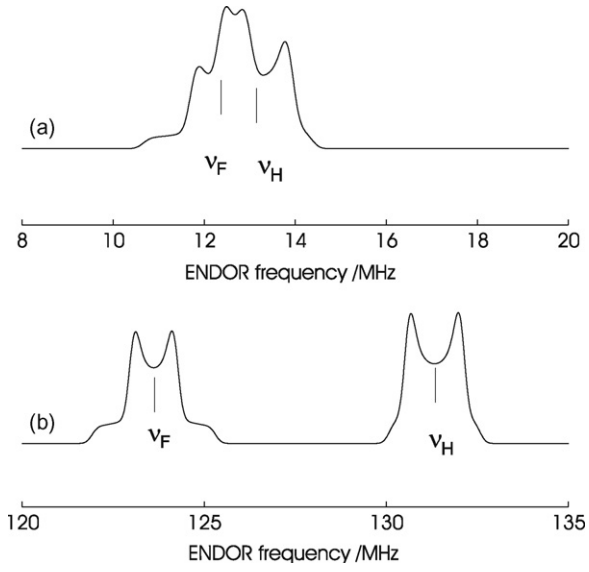

Fig. 5. Simulated ENDOR spectra of an unpaired electron ($S = 1/2$) interacting with a ^{19}F and a ^{1}H nucleus. $g = 2$, $\boldsymbol{A}(^{19}\text{F}) = [-1.2\ -1.2\ 3.4]$ MHz, $\boldsymbol{A}(^{1}\text{H}) = [-1.5\ -1.5\ 2.5]$ MHz. (a) X-band ENDOR spectrum. (b) W-band ENDOR spectrum. ν_F and ν_H stand for the nuclear Zeeman frequencies of ^{19}F and ^{1}H, respectively.

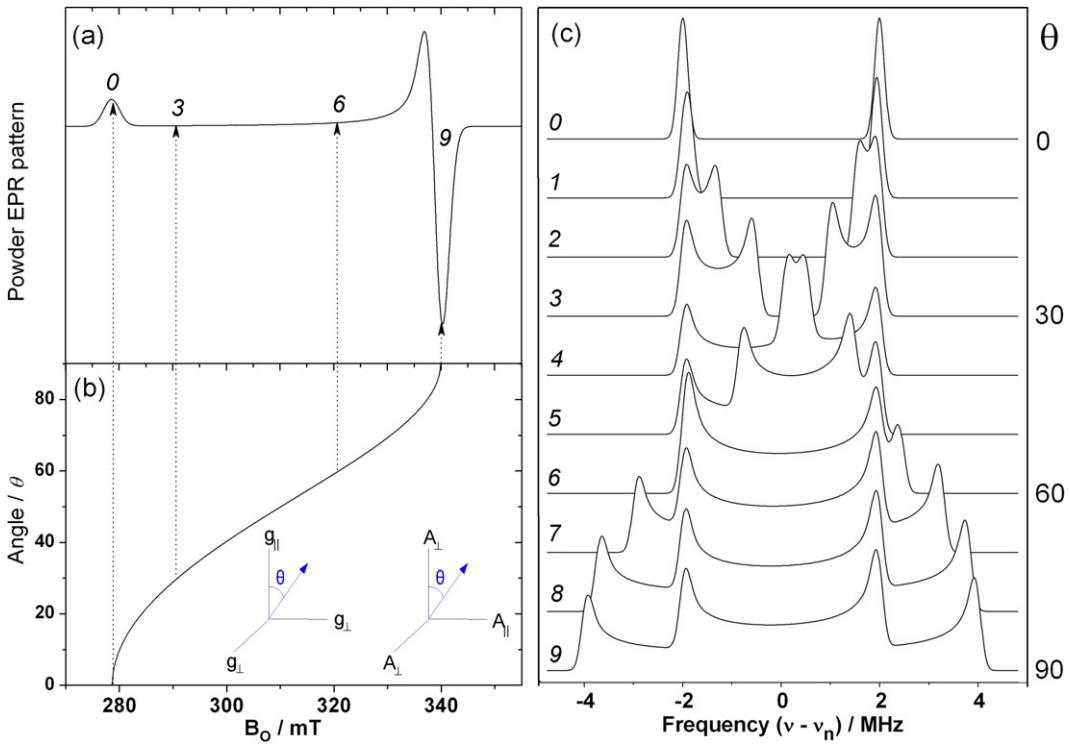

Fig. 6. Illustration of orientation selection. (a) Simulated X-band EPR spectrum of an $S = 1/2$ system with axial $\boldsymbol{g}$ tensor: $g_{||} = 2.43$, $g_{\perp} = 2.00$. (b) Calculated angular dependency curve for the $\boldsymbol{g}$ tensor. (c) Simulated ENDOR spectra if we assume that the electron spin from (a) is interacting with a ^{1}H nucleus, $\boldsymbol{A}(^1\mathrm{H}) = [-4.0\ -4.0\ 8.0]$ MHz. As the field position for the ENDOR measurement is changed in (a) (from positions 0, 1, 2, . . ., 9), the profile of the resulting ENDOR spectrum also changes in (c) due to the angular dependency of θ shown in (c) (where θ is the angle of B_0 with respect to the unique axis; see inset).

between an X-band and W-band ENDOR spectra resulting from weakly coupled ^{19}F and ^{1}H nuclei. While the contributions of both nuclei are overlapping at low frequency, as in the former case (Fig. 5a), the individual contributions are clearly separated in the latter spectrum (Fig. 5b) at higher frequency. However, in a number of experiments, such as some of the ESEEM experiments, higher frequency measurements may not be feasible due to technical reasons [20,24]. Nevertheless, it is clear from the previous discussion, that a multi-frequency approach will be crucial in order to unravel all nuclear interactions.

2.6. Solving the EPR puzzle

In order to obtain all of the available information in an efficient way, the EPR spectroscopist now has to choose between all the available experimental approaches. All EPR analyses will start with the detection of a CW-EPR spectrum, most often performed at X-band frequencies. This will immediately reveal some initial information on the $\boldsymbol{g}$ tensor and possible zero-field splitting. In some cases, additional high-field CW-EPR experiments will be needed. In a second step, some trial ESEEM, ENDOR or ELDOR-detected NMR experiments will be performed. Only for the cases with very small $\boldsymbol{g}$ anisotropy, will the microwave pulses excite the full EPR spectrum. In all other cases, only part of the spectrum is excited; namely the part corresponding to a narrow range around the observer magnetic field position. From Eq. (1), we know that a given g value leads, for a given microwave frequency, to an EPR resonance at a specific magnetic field position, B_0. Alternatively, a given magnetic field position will thus correspond to a specific g value, which is related to a specific orientation of the molecule with respect to the magnetic field (orientation dependence of the g values (Section 2.1)). Hence, the ESEEM, ENDOR or ELDOR-detected NMR spectrum performed at a fixed observer field, will only reflect the hyperfine and nuclear-quadrupole coupling corresponding to the selected orientation(s). This so-called orientation selection [41] concept is illustrated in Fig. 6 for a simple case of an unpaired electron interacting with a proton. The relative orientation of the $\boldsymbol{g}$ and $\boldsymbol{A}$ tensors is shown as inset in Fig. 6b. At position 0, only the orientations with $\theta = 0^\circ$ are selected (Fig. 6a and b). Hence, the ENDOR spectrum reflects the hyperfine ($A_\perp$) at this orientation (4 MHz splitting between the two peaks) (Fig. 6c). At position 9 all orientations with $\theta = 90^\circ$ are selected (*i.e.* all in-plane orientations) and the ENDOR spectrum now consists of contributions from the two extrema, $A_\perp$ (-4 MHz) and $A_{||}$ (8 MHz), and all hyperfine values lying between these values.

In order to reconstruct the full information (*i.e.* the full set of tensors), experiments at different field positions (and thus molecular orientations) need to be performed; this is a very time-consuming process. Hence, it is crucial to first select the optimal set of experiments based on some trial measurements, before starting the full orientation selection procedure. The EPR spectroscopist thus needs to have a high degree of specialization and a thorough knowledge about the available methods. This explains why the EPR technique cannot be used in a 'black-box' fashion. More technical and practical information on the appropriate choice of methods is highlighted elsewhere [42].

Once all of the EPR parameters are determined, they have to be translated into valuable electronic and geometric information. Several approaches ranging from very approximate methods to the combination of experiments with advanced quantum-chemical computations have been used [43,44]. In particular, the combination between EPR analyses and density functional theory (DFT) computations has led to interesting new insights [45–47]. In the following sections, some of the approaches introduced in the earlier sections will be highlighted using a number of representative examples.

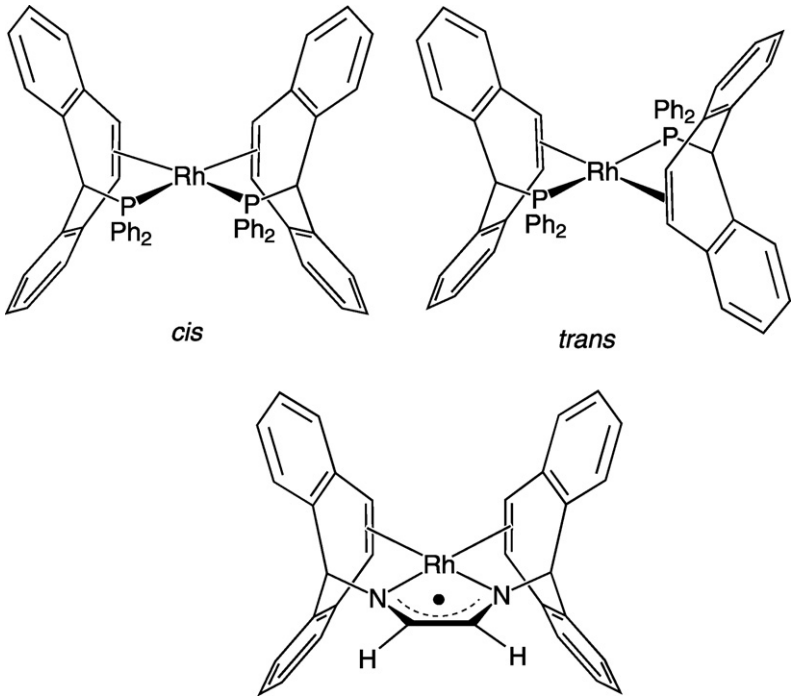

Fig. 7. Structure of the 17 electron *cis*- and *trans*-[Rh(tropp^{ph})$_2$] rhodium complex, and the [Rh(^{H}tropdad)](O$_3$SCF$_3$) complex [51,52].

3. Paramagnetic transition-metal complexes

Despite the important role that paramagnetic transition-metal ions play in synthetic homogeneous catalysis and inorganic chemistry, only a limited number of advanced EPR and ENDOR studies on metal complexes have been reported. This is surprising, given the fact that X-band CW-EPR has been used for a long time as a standard characterization technique for paramagnetic inorganic and organometallic compounds [25,48–50]. In this section we will illustrate the potential of the more advanced EPR studies using a selected number of studies on transition-metal complexes.

3.1. Rhodium complexes

Although complexes of rhodium in the formally low oxidation states of 0 and −1 are suggested to play an important role in hydroformylation and homogeneously catalyzed water splitting reactions, only a few of these complexes have been isolated to date. Grützmacher and co-workers succeeded in the synthesis of the 17-electron complex [Rh(tropp^{ph})$_2$] (tropp = tropylidene phosphane) (see Fig. 7) [51]. A combination of X-, Q- and W-band CW- and spin-echo-detected EPR, along with pulse ESEEM and ENDOR experiments, led to a full characterization of the complex [51]. The multi-frequency EPR spectra revealed contributions arising from both *trans* and *cis* isomers (Table 1). The temperature dependent CW-EPR study indicated a dynamic equilibrium between these isomers, whereby the *cis* isomer was slightly preferred ($\Delta H^{\circ} = -4.7 \pm 0.3$ kJ mol^{-1}) and a negative entropy ($\Delta S^{\circ} = -5 \pm 1.5$ J mol^{-1}) was found for the *trans*-[Rh(tropp^{ph})$_2$] ↔ *cis*-[Rh(tropp^{ph})$_2$] reaction. The fact that $g_x = g_y = g_{\perp} < g_z = g_{||}$ indicated the presence of either a distorted square planar structure (SOMO essentially $d_{x^2-y^2}$) or a compressed tetrahedron (SOMO essentially d_{xy}). Using two-dimensional Mims-ENDOR, the ^{103}Rh hyperfine values were determined (Table 1). Measurement of the ^{31}P, ^{13}C and ^{1}H hyperfine values of the ligand nuclei via CW-EPR, ENDOR and HYSCORE techniques revealed that the unpaired electron was primarily located on the metal centre. This seemingly contradicted the relatively small observed ^{103}Rh hyperfine coupling, but was explained by the counterbalance of the direct spin density in the higher lying orbitals and spin polarization in the core orbitals [51].

A similar approach led to the characterization of the water-stable rhodium complex [Rh(^{H}tropdad)](O$_3$SCF$_3$) (^{H}tropdad = 1,4-bis(5*H*-dibenzo[*a*,*d*]cyclohepten-5-yl)-1,4-diazabuta-1,3-diene) (see Fig. 7) [52]. The *g* and ^{103}Rh hyperfine values of this neutral and paramagnetic compound was clearly different from the ones found for the [Rh(tropp^{ph})$_2$] complexes (Table 2). DFT computations of different model complexes were performed and compared with the experimental ^{103}Rh, ^{14}N and ^{1}H hyperfine couplings determined via Q-band HYSCORE and ENDOR. This procedure left no doubt that the electronic structure was best described as [Rh^{+}(^{H}tropdad$^{\bullet -}$)], with the unpaired electron mainly localized on the ligand, explaining the difference with the tropp complexes (Fig. 7).

The [Rh(trop$_2$NCH$_2$)(PPh$_3$)] complex (trop = tropylidenyl) can in principle be described either as a rodazacyclopropane (with Rh in the formal oxidation state +1) or a rhodium iminium ion complex

Table 1
Principal *g* and ^{103}Rh hyperfine values for the different rhodium complexes mentioned in Section 3.1.

	g_x	g_y	g_z	A_x/MHz	A_y/MHz	A_z/MHz	Reference
trans-[Rh(tropp^{ph})$_2$]	2.030	2.030	2.050	19	19	23	[51]
cis-[Rh(tropp^{ph})$_2$]	2.0135	2.0135	2.030	16	16	20	[51]
[Rh(^{H}tropdad)]	1.9977	1.9977	2.0113	−10	−12	6	[52]
[Rh(trop$_2$NCH$_2$)(PPh$_3$)]$^{+}$	2.0145	2.0155	2.121	29	25	−18	[53]
[Rh^{I}(trop$_2$N$^{\bullet}$)(bipy)]$^{+}$OTf^{-}	2.0822	2.0467	2.0247	12	18	48	[56]

Table 2
Principal g values for the different paramagnetic MCR forms mentioned in Section 5.1.

	g_x	g_y	g_z	Reference
MCR_{red1a}	2.061	2.064	2.243	[123–126,128]
MCR_{red1c}	2.063	2.068	2.248	[125,126]
MCR_{red1m}	2.061	2.071	2.251	[125,126]
MCR_{ox1}	2.231	2.168	2.153	[128]
MCR_{red2a}	2.073	2.077	2.273	[129]
MCR_{red2r}	2.175	2.231	2.288	[129]
MCR + BPS	2.108	2.112	2.219	[120]
MCR + BrMe	2.093	2.093	2.216	[121]
MCR + IMe	2.101	2.101	2.212	[122]

(with Rh in the formal oxidation state −1) [53]. After electrochemical oxidation, this will then lead to a radical cation with the Rh centre either in a +2 or 0 oxidation state. A combined X- and Q-band CW-EPR, HYSCORE and HYEND (hyperfine-correlated ENDOR) study of the latter radical cation allowed for a determination of the ^{13}C, ^{103}Rh, ^{31}P and ^{1}H hyperfine couplings. The principal g and ^{103}Rh hyperfine values were clearly different from the previously observed complexes discussed in the previous sections (Table 1). The EPR parameters computed using DFT for the rhodaazacyclopropyl radical cation agreed very well with the experimental data. It was found that the assignment of an oxidation state to the metal centre in this radical was meaningless, since this radical is best described in terms of a delocalized unpaired electron (with 47% of the spin density on the rhodium centre, while the rest is on the ligand) [53].

Finally the free aminyl radicals, $NR_2^{\bullet}$, are known to play important roles in chemical and biological processes [54,55]. In this respect, the synthesis of a rhodium-stabilized aminyl radical by the Grützmacher group was very exciting [56]. By a mild one-electron oxidation of the amide complex of $[Rh^{I}(trop_2N)(bipy)]$ (bipy = 2,2′-bipyridyl and trop as defined before), a stable $[Rh^{I}(trop_2N^{\bullet})(bipy)]^{+}OTf^{-}$ complex was formed with OTf^{-} trifluorosulfonate. S-band (2.44 GHz) CW-EPR, Q-band pulsed ENDOR and Q-band HYSCORE experiments played a crucial role in the characterization of this compound [56]. In all of the studies mentioned above, the EPR techniques provided crucial information on the electronic nature of the complexes; this information was not easily accessible by any other spectroscopic method.

3.2. Paramagnetic metallo-porphyrin, corrin and phthalocyanine complexes

Metallo-porphyrin, corrin and phthalocyanine complexes are and have been extensively studied as model systems for many metalloproteins, such as heme and B_{12} proteins, and have also extensive applications ranging from catalysts and sensors to dyes and conducting materials, to name but a few [57–59]. Despite the difficulty involved in the preparation of these macrocycles, the applications of metallo-porphyrins in asymmetric catalysis, particularly cyclopropanation, have grown significantly in the last decade [60]. From the early years, X-band CW-EPR has been used to study these complexes, but only in recent years, have more advanced EPR tools been introduced in the analysis of these systems [61]. One of the authors of this review has performed multi-frequency EPR analyses of different paramagnetic transition-metal porphyrin, corrin and phthalocyanine complexes [62–70], and some illustrative and representative examples will be described in more detail below.

Although it has long been known that the intramolecular dimethylbenzimidazole base does not coordinate to the Co^{II} ion of cobalamin (B_{12r}) at low pH, there has been much discussion about the actual coordination number of the cobalt ion in this form. Four-coordination, five-coordination (involving one water molecule) and six-coordination (with two axial waters) modes have all been proposed [71–73]. A detailed multi-frequency EPR and ENDOR analysis of B_{12r} at low pH, and of the model complex heptamethyl cobyrinate perchlorate (cobester), revealed important information about the axial ligation of Co^{II} corrinate complexes [67]. When cobester was dissolved in an apolar solvent, a contact-ion pair was found to be formed between the Co^{II} complex and its counter ion, perchlorate. In methanol, the axial ligation of the cobester complex was temperature dependent and correlated with the phase transition of the solvent, as indicated by the temperature dependence of the CW-EPR spectra. In the α crystalline phase of methanol, only one methanol molecule coordinated to the cobaltous complex, whereas two methanol molecules coordinated in the glassy state. When a H_2O:methanol mixture is used as a solvent, the frozen solution has a largely crystalline structure, even at low temperature, and, hence, only the EPR spectrum of the five-coordinated species could be observed in this case. Solvent coordination could be determined unambiguously using X- and W-band ENDOR, in combination with ^{2}H isotope labelling. The DFT computations of the EPR parameters of five- and six-coordinated Co^{II} corrinates corroborated the experimental interpretations. The study showed the huge influence that the phase-transition properties of the solvent can have on the structure of transition-metal complexes, and this is a very important consideration in the investigation of more complex catalyst–solvent–substrate mixtures.

In a similar way, the subtle effect that the matrix has on the electronic state of Cu^{II} phthalocyanine complexes could be revealed from a combined DFT and multi-frequency CW- and pulsed EPR study [69]. The small changes in the EPR and ENDOR spectra observed when copper(II) 2,9,16,23-tetra-*tert*-butyl-29*H*,31*H*-phthalocyanine ($CuPc^{t}$) was dissolved in toluene or in sulphuric acid, could be interpreted in terms of a more covalent metal-ligand σ bonding in the toluene case. The solvent matrix was found to have a much stronger effect on the electronic structure of the Cu^{II} core of the phthalocyanines than the ring substituents. Given the fact that the unpaired electron resides predominantly in the copper $d_{x^2-y^2}$ orbital, the effect of the matrix molecules on the spin-density distribution is small. In contrast, the spin-density distribution in Co^{II} phthalocyanines is strongly affected by the surroundings (unpaired electron is in a d_{z^2} orbital) [68].

4. Homogeneous asymmetric catalysts

In the previous section, examples have been given on the extraordinary capabilities of EPR to explore the metal centre and its local surroundings in paramagnetic transition-metal complexes. In this section, we focus on EPR applications in the important field of homogenous asymmetric catalysis. The amount of research on enantioselective chiral catalysts by EPR is rather scarce and many of the reported works only make use of the conventional CW-EPR mode, mostly in a limited or incidental way. In this section we will therefore review some of the most relevant extended EPR/ENDOR investigations reported on chiral catalysts.

4.1. The early days—a chiral oxovanadium complex

One of the first reported investigations that showed the great potential of applying pulsed EPR and ENDOR techniques to the study of chiral transition-metal-containing catalysts was conducted by Schweiger and co-workers [74]. They explored the coordination sphere of *cis*-oxovanadium(IV) bis((1*R*)-3-(heptafluorobutyryl)camphorate) (**1**), a catalyst used for the hetero Diels–Alder reaction of an aldehyde with an activated diene to form pyrone derivates with high enantioselectivities (up to 85% *ee*) and diastereoselectivities (98–99%) [75].

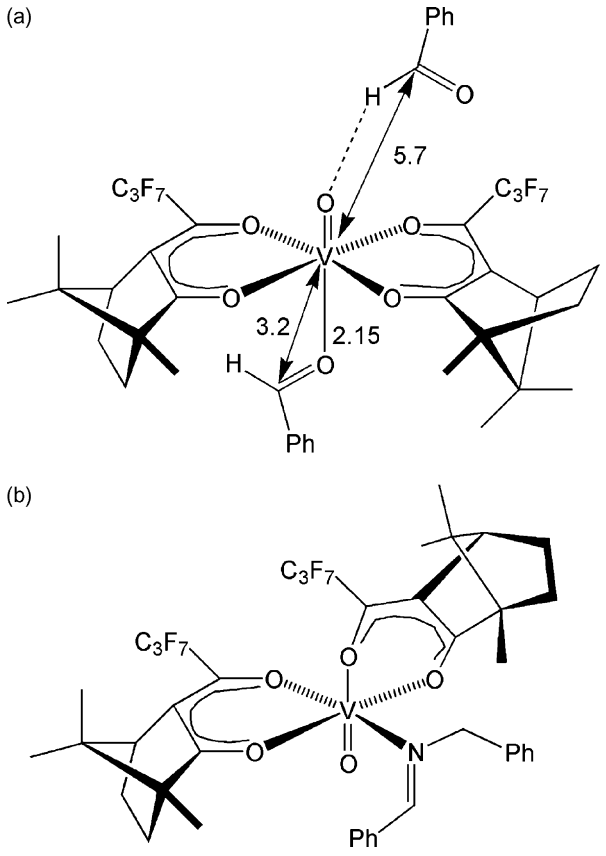

Fig. 8. Geometry and structural parameters obtained from the pulsed EPR and ENDOR study of oxovanadium(IV) bis((1*R*)-3-(heptaflurobutyryl)camphorate) (**1**) ligated to (a) benzaldehyde and (b) *N*-benzyliden-benzylamine. For the first complex, internuclear distances determined from the experiments are indicated (values in Å).

The X-ray study revealed that complex (**1**) adopted a trimeric form in the solid state. The trinuclear oxo-bridged cluster $(\mathbf{1})_3$ consists of three equivalent units with C_3 symmetry. This gave no information about either the actual conformation of the catalyst in solution or the structure adopted upon aldehyde or amine coordination. The X-band CW-EPR experiments of (**1**) in toluene revealed the typical EPR signature of a vanadyl ion in a d_{xy} ground state (analogous to that shown in Fig. 2a). The addition of benzaldehyde to the solution produced only a small reduction in the hyperfine couplings, suggesting axial binding of the aldehyde. Instead, addition of *N*-benzyliden-benzylamine resulted in a larger decrease of the hyperfine constants and indicated the substitution of an in-plane oxygen by the imine nitrogen. Confirmation of these suggestions about the binding site and coordination of benzaldehyde and *N*-benzyliden-benzylamine could be determined using different ENDOR and ESEEM techniques.

By recording the ^{13}C X-band Mims-ENDOR spectra at different magnetic field positions for (**1**) coordinated with single-^{13}C-labeled benzaldehyde ($^{12}C_6H_5$–^{13}CHO), it was possible to determine the hyperfine coupling constants of the labeled carbonyl carbon and its relative orientation in space with respect to the vanadyl centre. Two types of ^{13}C interactions were detected. The first one was assigned to the aldehyde carbon at a distance of ∼5.7 Å. It agreed with a hydrogen bonding of the benzaldehyde to V=O (Fig. 8a). The second ^{13}C coupling originated from a benzaldehyde axially coordinated to the vanadium atom. From the dipolar part of the hyperfine coupling, a VO–C distance of 3.20 Å was determined. On the basis of geometrical calculations, and assuming that the C=O distance is typically 1.24 Å, the V–O=C angle and V–$O_{aldehyde}$ distance were found to be 140° and 2.15 Å, respectively. This spatial conformation (Fig. 8a) is characteristic of η^1-coordinated carbonyl compounds. The two- and three-pulse ^{14}N ESEEM spectra of *N*-benzyliden-benzylamine coordinated to (**1**) revealed a mostly isotropic ^{14}N hyperfine coupling (∼5.2 MHz). The magnitude was typical for a nitrogen equatorially bound to the vanadium atom and indicated that the imine ligand was binding in a *cis* mode (Fig. 8b). This work nicely illustrates how spatial information on the nature of interacting substrates (of vital importance when probing asymmetric induction steps) can be explored by advanced EPR techniques.

4.2. Chiral Schiff-base complexes

Metal–salen complexes based on Ti, V, Cr, Mn, Fe, Ru and Co have been extensively used over the years as catalysts for the oxo functionalization of organic substrates [76]. The oxo-transfer species in these transformations is believed to be based on a terminal metal-oxo, metal-peroxo or bridging oxo complex. The salen ligand is most widely used for this reaction owing to the ease of preparation/derivatization and the rigid tetradentate binding motif, reminiscent of the porphyrin framework in heme-based oxidative enzymes. A major breakthrough occurred in 1990 with the discovery of chiral manganese(III) salen catalysts by the groups of Jacobsen [77] and Katsuki [78,79] for the epoxidation of unfunctionalized olefins. Jacobsen and co-workers introduced a new $Mn^{III}Cl$ derivative of the chiral salen-type Schiff base ligand *N*,*N*′-bis(3,5-di-*tert*-butylsalicylidene)-1,2-cyclohexane-diamine (**2**) (Fig. 9a), which converts achiral alkenes into chiral epoxides with enantioselectivities as high as 98% [77]. This so called Jacobsen catalyst was '1994 Reagent of the year' and is one of the best chelating agents known to date. Remarkably, not only Mn, but also other transition-metal complexes of (**2**) have shown astonishing enantiomeric excesses in the epoxidation of unfunctionalized alkenes, epoxide ring opening, hydrolytic kinetic resolution of racemic epoxides, cyclopropanation and trimethylsilylcyanation of aldehydes [80]. Nevertheless, and even though they are commercially available catalysts, the origins of their striking selectivity are not yet fully understood. In particular, questions remain concerning the nature of the oxo-transfer species, the mode of efficient stereochemical communication between catalysts and substrate, and how variations in ligand substituents can tune the catalytic activities. In this section, we will discuss some of the most representative articles about CW-EPR, CW-ENDOR and pulsed EPR/ENDOR applied to the study of different metallo-salen complexes, which have tried to explore these questions.

4.2.1. Manganese

Regarding the high enantioselectivity of the [MnCl(**2**)] complex, a two step catalytic cycle involving the formation of active Mn^{V}=O species by an oxidizing agent was initially suggested by Kochi and co-workers [81]. Since then, several attempts to identify these and other intermediate species have been reported in order to understand this very efficient asymmetric epoxidation process. For a thorough account of this chemistry of Mn–salen derivatives, the reader is referred to an excellent review by Katsuki [79].

Bryliakov et al. studied the reactive intermediates of several catalyzed [MnCl(**2**)] asymmetric epoxidations by X-band CW-EPR [82–85]. Specifically, they monitored the interaction of [MnCl(**2**)] with iodosylbenzene (PhIO), *m*-chloroperbenzoic acid (*m*-CPBA), isobutyraldehyde (IBA), pivalaldehyde, peroxyisobutyric acid (PIBA), IBA/*N*-methylimidazole (*N*-Me-Imd) and *m*-CPBA/*N*-methylmorpholine-*N*-oxide (NMO). The X-band CW-EPR spectra of [MnCl(**2**)] in toluene or CH_2Cl_2 at 77 K exhibited similar features

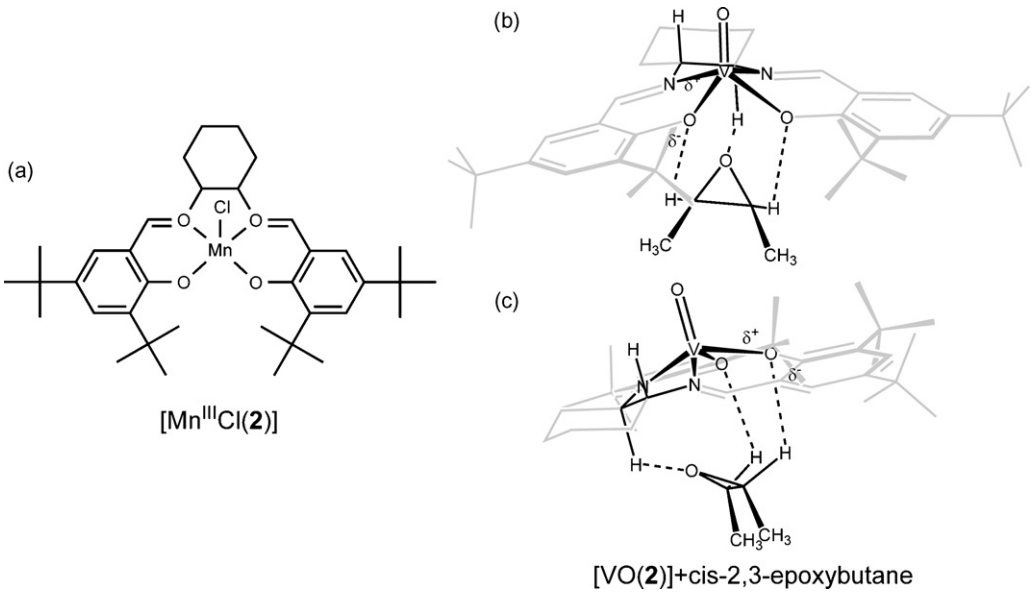

Fig. 9. (a) Chemical structure of [Mn^{III}Cl(**2**)]. (b and c) Schematic illustration, from two different orientations, showing the hydrogen bonds (dashed lines) and coordination mode of *cis*-2,3-epoxybutane to [VO(**2**)] as obtained from ENDOR and DFT [91].

dominated by a broad signal at $g \sim 7.8$ from forbidden transitions within the $|m_S = \pm 2\rangle$ non-Kramers doublet of mononuclear Mn^{III} ($S = 2$) [82–85]. The [MnCl(**2**)] complex was found to be very sensitive to the ligand coordination and this was translated into clear changes in the EPR spectrum. Upon addition of IBA, PIBA or pivalaldehyde [84,85], the Mn^{III} signal at $g \sim 8$ was transformed into a superposition of signals at $g \sim 5.2$ assigned to mononuclear Mn^{IV}=O–L with different axial ligands (L = Cl^-, $RCOO^-$, *etc.*). This was accompanied by the appearance of spectral contributions originating from a Mn^{II} complex. All the manganese was converted into Mn^{IV} by exposing the sample to air. Addition of *trans*-β-methylstyrene at this point showed no epoxide, meaning that [Mn^{IV}(**2**)] could not be the species responsible for olefin epoxidation. However, if *trans*-β-methylstyrene was included before the oxidants, a 31% and 45% epoxide formation yield was achieved for PIBA and IBA/O_2 respectively. This led the authors to tentatively suggest that the actual species behind the epoxidation process was a short lived Mn^{III} acylperoxo complex, which could not be detected because of its high reactivity towards alkenes or fast conversion into oxo Mn^{IV}.

When *N*-Me-Imd was introduced into the solution, to obtain the MnCl(**2**)/IBA/*N*-Me-Imd/O_2 catalytic system in the presence of *trans*-β-methylstyrene, three different signals were detected [84]. The authors linked these signals to a *N*-Me-Imd-Mn^{IV}(OOCOR) acylperoxo complex, a *N*-Me-Imd-Mn^{IV}=O(**2**) adduct and a bis-μ_2-oxo-Mn^{III}/Mn^{IV} dimeric complex bound to two axial *N*-Me-Imd ligands. No pulsed EPR or ENDOR experiments were performed to support these conclusions and, in some cases, the assignments were purely hypothetical. Since both the dimeric and the *N*-Me-Imd-Mn^{IV}=O(**2**) complexes were not capable of epoxide formation, the authors suggested that the proposed acylperoxo complex was responsible for the catalytic reaction. Similar conclusions were drawn from the reactions with NMO and *m*-CPBA [82]. The acylperoxo species could be directly involved in the epoxidation process or be the precursor of a Mn^{V}=O species by homolytic cleavage of the O–O fragment of the acyl ligand.

Campbell et al. introduced the use of dual-mode X-band CW-EPR to study the epoxidation of *cis*-β-methylstyrene by *R*,*R*-[Mn^{III}Cl(**2**)] [86]. Parallel polarization EPR is helpful for integer electron spin systems like Mn^{III} ($3d^4$, $S = 2$), whereas the more conventional perpendicular polarization EPR enables the study of half integer spin systems. The potential of this technique was already successfully demonstrated in the study of manganese-containing biosystems [87]. The [MnCl(**2**)] study revealed that the additives NMO and 4-phenylpyridine-*N*-oxide (4-PPNO), commonly used to improve the epoxidation yields and enantioselectivity, bind to the Mn^{III} centre *before* the epoxidation reaction. The use of the dual mode EPR allowed the identification of different intermediate manganese complexes that cannot be correctly assigned in a conventional EPR experiment. A correlation between the formation of a $Mn^{III,IV}$ dimeric cluster and the epoxidation reaction could be determined. The EPR data of the individual species could be linked to the inner-coordination sphere of the manganese ion and give an insight into the mechanistic aspects of catalyst degradation and formation of unwanted byproducts.

Finally, a CW-EPR study by Hsieh and Pecoraro [88] suggested that the reaction of [Mn^{III}Cl(**2**)] with *m*-CPBA leads to the formation of meta-chlorobenzoate (*m*-CBA) by oxygen transfer to the [Mn^{III}Cl(**2**)] complex. The organic radical observed in the EPR spectra may be attributed to a chlorobenzo-carboxyl radical formed by reaction with the Mn^{V}=O species. Since this means that Mn^{V}=O can undergo single electron reduction, this poses the question whether it can be assumed that Mn^{V} species act via an oxo transfer group or not. Campbell et al. [86] also detected formation of an organic radical but thought this might be a byproduct formed due to the oxidizing strength of *m*-CPBA, since it was not formed when NaOCl was used instead of m-CPBA.

It is clear from the above review on [MnCl(**2**)] enantioselective epoxidation that relatively simple CW-EPR experiments, both in the conventional and dual mode, can shed some light on the reaction mechanism. However, many questions still remain open. The use of advanced pulsed EPR/ENDOR techniques could significantly contribute to a rapid enhancement in our knowledge of the mechanistic details of these systems, as will become shown in Sections 4.2.2 and 4.2.3 for related complexes. However, for the high-spin Mn^{III} system treated in this section, the expected short longitudinal relaxation times (T_1) and high-spin-related effects may pose a limit to the applicability of some of the pulsed EPR and ENDOR methods. In this context, it is important to point out one of the most important limitations of these spectroscopic methods. For

very short relaxation times, ESEEM and pulsed ENDOR may not be feasible, because the signal is decaying too fast (sometimes even within the spectrometer's deadtime). In order to maximally slow down the different relaxation mechanisms, pulsed EPR and ENDOR measurements are therefore performed at very low temperatures (4–25 K region). Pulsed EPR and ENDOR measurements thus have the drawback that the catalyst, or more generally the paramagnetic system of interest, is not studied at its normal working temperature. Only an experimental evaluation can reveal whether a pulsed EPR or ENDOR analysis is feasible for [MnCl(**2**)] and whether some of the problems can be circumvented by the use of more advanced multi-frequency pulsed EPR methods, as one of us recently showed for high-spin Fe^{III} systems [39,89].

4.2.2. Vanadium

In a pair of communications, some of the co-authors of this review have shown the effectiveness of combining CW-ENDOR and DFT calculations to study chiral vanadyl Schiff-base complexes [90,91]. The authors explored the spatial conformation and weak chiral interactions between [VO(**2**)] and selected epoxide substrates, epoxypropane and 2,3-epoxybutane. Although vanadium-based complexes, including Schiff bases, are widely reported for efficient asymmetric oxidation reactions [92] and multi-electron redox catalysts [93], the [VO(**2**)] system was originally used as a model of the [MnCl(**2**)] and [Co(**2**)] catalysts, to investigate the mode of chiral induction by weak outer sphere interactions between the ligand and an epoxide substrate [71,72].

^{1}H CW-ENDOR of [VO(**2**)] in non-coordinating (toluene) and weakly coordinating solvents (CH_2Cl_2 and DMF) showed ^{1}H couplings assigned to the salen-based ligand, namely (i) the two cyclohexyl methine protons ($H_{methine}$–VO distances of 3.05 Å and 3.46 Å), (ii) the imine protons (H_{imine}–VO distance ≈4 Å) and (iii) the inner 6-*tert*-butyl protons (H_{butyl}–VO distance ≈3.43–4.05 Å; range due to rotamers) [90]. These results were found to be in good agreement with the DFT computations. Additional peaks arose in the spectra following epoxide coordination and were assigned to the epoxide ring vicinal protons. Different epoxide ^{1}H ENDOR couplings were found for the pairwise combinations of *R*,*R*-[VO(**2**)]/*R*-epoxypropane and *R*,*R*-[VO(**2**)]/*S*-epoxypropane [90], indicating different conformations of the diastereomeric adducts. Furthermore, the similarity of the *rac*-[VO(**2**)]/*rac*-epoxypropane and *R*,*R*-[VO(**2**)]/*R*-epoxypropane spectra revealed that the homochiral *R*,*R*–*R* adduct was strongly preferred. Based on a point dipolar approximation, the two vicinal proton $H_{epoxide}$–VO distances obtained were 3.72 Å and 3.56 Å for *R*,*R*–*R*, and 3.76 Å and 3.66 Å for *R*,*R*–*S*, due to the asymmetric binding mode of the epoxides. These results were confirmed by DFT. Recently, it was suggested that the key step in the hydrolytic kinetic resolution of epoxides by [Co(**2**)](X) (X = anion) is the interaction of activated [Co(**2**)–(H_2O)(OH)] and [Co(**2**)–(H_2O)(epox)] complexes and not the enantioslective binding of the epoxide [94]. The above ENDOR study supports this, since a preferential formation of the homochiral diastereomeric *R*,*R*–*R* or *S*,*S*–*S* adducts was found. If these are involved in the hydrolysis step, the opposite enantiomers will be observed as products.

The ^{1}H CW-ENDOR spectra of *rac*-[VO(**2**)] in *trans*-2,3-epoxybutane and *cis*-2,3-epoxybutane were also recorded; the former system displayed signals identical to the non-coordinated *rac*-[VO(**2**)] complex in toluene suggesting the *trans*-isomer was unbound. In the *cis* case, the ^{1}H hyperfine couplings from the vicinal protons of the epoxide were translated into VO–$H_{epoxide}$ distances of 3.30 Å and 3.97 Å. Confirmation of the selective coordination of the *cis* epoxide was obtained by a competitive *rac*-[VO(**2**)]/*rac*-2,3-epoxybutane experiment, which produced an ENDOR spectrum identical to that of the pure *cis* isomer. Interestingly, the DFT model exhibited hydrogen-bond interactions between the vicinal epoxide protons and the two phenoxide oxygen atoms from the salen ligand, in addition to a H-bond between the epoxide O atom and the methine H^{exo} proton attached to the asymmetric C-backbone (Fig. 9b and c). The latter interaction is crucial in determining the magnitude of the weak electrostatic coordination in the [VO(**2**)]/epoxide complex, and therefore the enatioselectivity. The hydrogen bonds formed between catalyst and epoxide could help to orient the transition-state intermediates. The hydrogen-bond formation with the phenoxide donors may be enhanced in electron-rich ligands, which may explain the excellent enantioselectivities observed in catalyst like [MnCl(**2**)].

4.2.3. Cobalt

In our recent work [95], we used pulsed EPR techniques, in combination with DFT calculations, to study the electronic nature of the widely employed [Co^{II}(**2**)] complex, which is an excellent catalyst for the hydrolytic kinetic resolution of racemic epoxides (after activation under air with an organic acid) [96]. The spin Hamiltonian parameters obtained from the X-band CW-EPR spectra of a *R*,*R*-[Co(**2**)]/toluene frozen solution were consistent with a $|yz, {}^2A_2\rangle$ ground state. The X-band ^{14}N HYSCORE experiments revealed the hyperfine and nuclear-quadrupole tensors of the nitrogens from ligand (**2**). The relative orientation of these tensors in the molecular frame could only be determined by matching the experimental data to DFT computations. X-band proton HYSCORE allowed for a determination of the proton hyperfine values of the cyclohexyl methine protons, which were clearly different from the protons of the ethylenediimine bridge in *N*′,*N*-ethylene-bis-(acetylacetoatiminato) cobalt(II). The EPR data of the pre-activated [Co(**2**)] complex provided a reference basis to follow the evolution of the electronic and geometric structure of the catalyst under acid activation. In a first step, the activation of the cobalt catalyst with acetic acid in anaerobic conditions was tested [95]. This induced an enormous change in the CW-EPR spectra. Two new signals were observed that could be related to (a) the binding of [Co(**2**)] complex to an axial σ-donor, most likely acetate, and (b) a high-spin ($S = 3/2$) [Co^{II}] species related to the destruction of [Co(**2**)] and possible formation of $Co(OAc)_2$-based complexes.

4.2.4. Chromium

Although the field of enantioselective epoxidation of alkenes is dominated by [MnCl(**2**)], [CrCl(**2**)] is also a very effective catalyst for epoxidation of *E*-alkenes. While the various oxidation states of Cr can be readily investigated by low and high field EPR [8], it is surprising that so few EPR studies have actually been conducted on [CrCl(**2**)]. Bryliakov et al. [97,98] performed a CW-EPR study on [CrCl(**2**)] and a derivative complex, namely *racemic*-*N*,*N*′-bis(3,4,5,6-tetra-deutero-salicylidene)-1,2-cyclohexanediamino Cr^{III} chloride. Both complexes showed effective *g* values of $g \approx 4$ and 2, typical of an electronic $S = 3/2$ spin system, while the zero-field splitting parameters revealed moderately large *D* values (∼0.7–0.8 cm^{-1}) and small rhombicity parameter, *E* (∼0.108–0.042 cm^{-1}). A notable decrease in the axial zfs parameter and an increase in the rhombicity parameter were observed after addition of pyridine as an activator. This revealed that the EPR parameters were sufficiently sensitive to monitor changes to the structure of the catalysts before and after activation.

At least two intermediates species were identified by CW-EPR when the [CrCl(**2**)] complex was reacted with iodosylbenzene (PhIO). CW-EPR and ^{1}H NMR revealed that the first intermediate could be assigned to a reactive mononuclear oxochromium(V) species [$Cr^{V}O$(**2**)L], where L = Cl^- or a solvent molecule. The second intermediate was identified as an inactive mixed-valence binuclear [L(**2**)$Cr^{III}OCr^{V}$(**2**)L] complex. Bryliakov et al. thereby proposed that the [CrCl(**2**)] catalyzed epoxidation of alkenes proceeds in accordance with a modified "oxygen rebound cycle" [97,98].

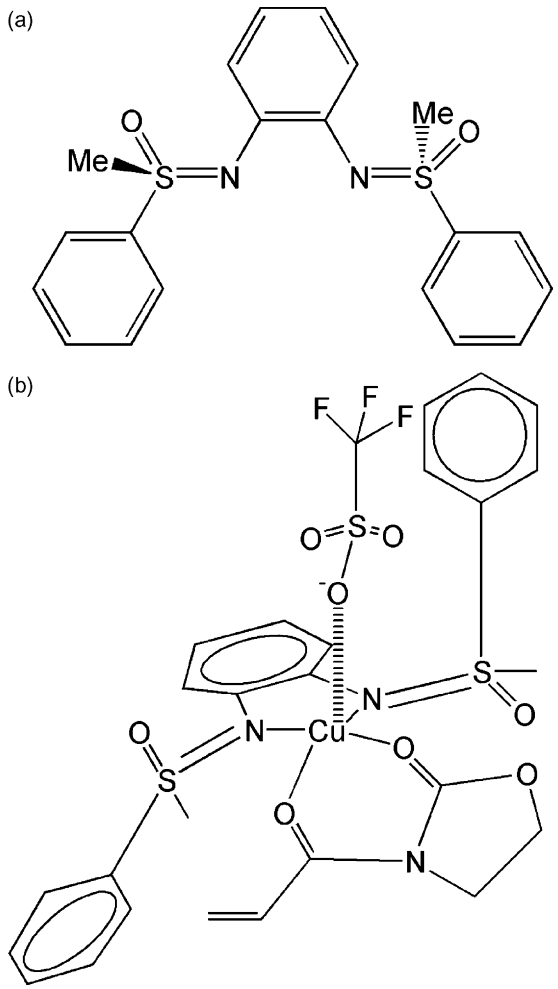

Fig. 10. (a) Chemical structure of the bis(sulfoximine) ligand *S*,*S*-(**3**). (b) Schematic representation of the geometry of Cu^{II} complex (**4**) as obtained from the EPR/ENDOR analysis in Ref. [100].

4.3. Copper(II) bis(sulfoximine) and bis(oxazoline) complexes

It has recently been reported that copper complexes of the bis(sulfoximine) ligand (**3**) (Fig. 10a) can catalyze asymmetric hetero Diels–Alder reactions with high enantioselectivities (99% *ee*) [99]. Bolm et al. identified a Cu^{II} complex (**4**) (Fig. 10b) associated with the catalyzed Diels–Alder reaction [100]. This complex was formed by reaction of (**3**) with copper triflate ($Cu^{II}(OTf)_2$), and its additional activation with a dienophile. Evidence for this proposed structure was obtained using a combination of different CW- and pulsed EPR techniques. The principal *g* and copper hyperfine values, obtained by X- and W-band CW-EPR, were typical for a tetragonally distorted pyramidal Cu^{II} centre with $d_{x^2-y^2}$ ground state. A partially resolved hyperfine splitting revealed the coupling to two ^{14}N nuclei. These couplings were determined more accurately using hyperfine-contrast selective Davies-ENDOR and are typical of equatorially bonded nitrogens. The W-band Mims-ENDOR spectra displayed orientation dependent ^{19}F hyperfine interactions stemming from ^{19}F nuclei at ~5 Å corresponding to a triflate anion in an axial coordination position. X-band HYSCORE experiments revealed further interactions with ^{1}H, ^{19}F, ^{13}C, ^{14}N, and possibly $^{35}Cl/^{37}Cl$ nuclei. The ^{1}H signal was tentatively attributed to protons from the sulfoximine ligand with proton hyperfine couplings lower than 10 MHz, while the ^{19}F coupling confirmed the ENDOR result. Furthermore, the authors observed contributions from ^{13}C nuclei in natural abundance, from the ^{14}N nucleus of the dienophile ligand, and from $^{35}Cl/^{37}Cl$ nuclei from the CH_2Cl_2 solvent. The combination of CW and pulsed EPR/ENDOR techniques showed a low symmetry of complex (**4**) with a distorted geometry of the copper centre coordinated axially to the triflate ligand. The remote ^{14}N observed with HYSCORE, together with preliminary molecular-mechanics calculations, suggested the coordination of the dienophile activator through non-equivalent in-plane oxygen atoms.

The effect of the counter ions on the stereoselectivity of the Diels–Alder reaction catalyzed by [Cu(**3**)] was also studied by EPR techniques [101]. The complexes formed between the parent $Cu^{II}X_2$ (X = Cl, Br, OTf and SbF_6) salts, *S*,*S*-(**3**) and *N*-(1-oxoprop-2-en-1-yl)oxazolidin-2-one as substrate in CH_2Cl_2 were investigated. The *ee* was 75% in the presence of TfO^- and SbF_6^-, and no selectivity was observed for the Cl^- and Br^- counterions. This difference in enantioselectivities was also reflected in the EPR spectra. The X-band CW-EPR spectra of *S*,*S*-[Cu^{II}(**3**)]–$(X)_2$ with X = TfO^- and SbF_6^- were analogous and produced comparable axial *g* and *A* copper hyperfine values. The spectra of X = Cl^- and Br^- were similar and consisted of contributions from a single and coupled Cu^{II} species. The formation of oligonuclear copper compounds was indicated by the observation of a 6-line hyperfine structure and a half-field signal. From the latter signal, the authors estimated a Cu^{II}–Cu^{II} distance of ~6 Å for the dinuclear *S*,*S*-[Cu^{II}(**3**)]–$(X)_2$ complexes (X = Br^- and Cl^-). The remarkably long Cu–Cu distance, compared with those reported for crystalline (solvent free) halogen-bridged Cu complexes, suggested that axial chlorine atoms of CH_2Cl_2 are implicated in the bridge.

Activation of the catalyst with the above mentioned dienophile had again parallel effects on the CW-EPR spectra of TfO^- and SbF_6^-, and of Cl^- and Br^-. The activated catalyst gave almost identical spectra in the presence of TfO^- and SbF_6^- with a better resolution than their precursors. In the Cl^- and Br^- case, the EPR spectra consisted of two contributions from single and coupled Cu^{II} species, respectively.

To analyze the single copper species in more detail, X-band Davies-ENDOR and HYSCORE experiments were performed on *S*,*S*-[Cu^{II}(**3**)]–$(X)_2$ with X = Br^- and Cl^-. Strongly coupled ^{14}N and $^{35}Cl/^{37}Cl$, as well as weakly coupled ^{1}H were detected by ENDOR and HYSCORE. None of these spectra changed upon addition of the dienophile activator. This demonstrates that the dienophile substrate does not bind strongly. The study revealed that, in the case of the TfO^- and SbF_6^- counterions, the asymmetric coordination sphere of the [Cu^{II}(**3**)] complex was formed by two equatorial inequivalent N atoms and two counterions, which moved to axial sites when replaced by the dienophile substrate. For the strongly coupled Br^- and Cl^- counterions in equatorial positions, the dienophile could only replace the weakly bound axial solvent molecules. This was supported by the intensity decrease observed for the dimeric signal in the CW-EPR spectrum and was consistent with the idea that Cu–Cu interactions take place through the axially coordinated halogen atoms. Stereoselectivity thus requires weakly coordinated counterions that can be displaced by the substrate and moved to axial positions.

Other analogous complexes equally successful at bidentate coordination of Cu^{II} in an asymmetric environment for a range of reactions include the bisoxazolines [2,102] and phosphinooxazoline ligands [103]. A significant amount of research has been devoted to the immobilization of the bisoxazolines for asymmetric heterogeneous catalysis [104,105], particularly those containing coordinated Cu^{II} ions. Despite this, relatively few EPR investigations have been carried out. Using CW-EPR, Traa et al. studied the enantioselective aziridination of styrene inside a CuY zeolite using the complex (*S*)-(−)-2,2′-isopropylidenebis(4-phenyl-2-oxazoline) [106]. The EPR spectra were consistent with the formation of a single Cu^{II}–bisoxazoline complex per supercage, and notable changes were observed in the spectra during the

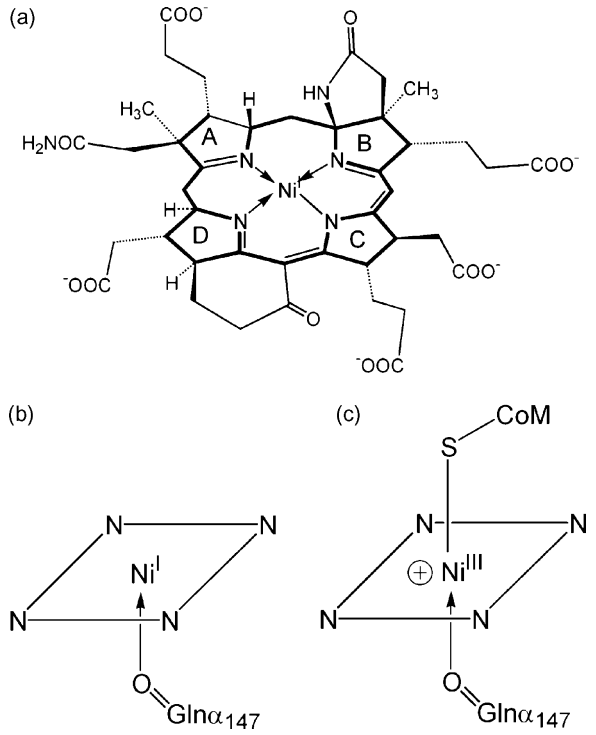

Fig. 11. (a) The nickel-porphyrinoid co-factor F_{430} responsible for the MCR activity. (b) A schematic representation of the structure of the nickel core in MCR_{red1a} as determined by EPR [123–126]. (c) A schematic representation of the structure of the nickel core in MCR_{ox1} as determined by EPR [128].

course of the reaction with styrene and the nitrogen source (*N*-(*p*-tolylsulfonyl)iminophenyliodinane).

5. Biological catalysts–enzymes

Many of the complexes mentioned in Sections 3 and 4 have been inspired by nature or used to model active sites in metallo proteins. Indeed, nature is the ultimate master of asymmetric synthesis, employing enzymes to catalyze stereoselective reactions with unparalleled specificities. Advanced EPR techniques are often used to extract valuable information about the paramagnetic cores of transition-metal-binding biomolecules, which contrasts the limited applications of these methods in synthetic inorganic catalysis. We mention here only a few studies that deal with the use of EPR to elucidate the catalytic cycle of methyl-coenzyme M reductase (MCR). We believe that these examples will be interesting also to the general inorganic-chemistry community and that the spectroscopic approaches can be extrapolated to applications in coordination chemistry and homogeneous catalysis in general. More extended reviews on the applications of advanced EPR methods in the study of metallo proteins can be found elsewhere [21–24,107–109].

5.1. The active site of methyl-coenzyme M reductase

It has long been established that methanogenic *archaea* extract energy via a specific metabolic pathway converting C_1 substrates, such as CO_2 or acetate, to methane [110]. The most important step in this reaction is the reduction of methyl-coenzyme M (2-(methylthio)ethane sulfonate, CH_3–S–CoM) with coenzyme B (7-thioheptanoyl-threoninephospate, HS–CoB) to CH_4 and Co–M–S–S–CoB. This reaction is catalyzed by MCR, an enzyme with two structurally interlinked active sites that contain the nickel porphinoid cofactor F_{430} (Fig. 11a) and are embedded in an $\alpha_2\beta_2\gamma_2$ subunit structure. Since the currently available X-ray structures of MCR all describe the inactive, oxidized Ni^{II} forms [111–113], EPR provides a main characterization tool to explore the different paramagnetic forms of MCR, including the enzymatically active ones.

Two catalytic mechanisms have been proposed for the methane-forming step, both starting from the $Ni^{I}F_{430}$ form. In the mechanism *A*, a methyl transfer from CH_3–S–CoM to $Ni^{I}F_{430}$ yielding a CH_3–$Ni^{III}F430^{+}$ compound has been proposed followed by a protonolysis step to form methane [114–117]. The second mechanism *B* proposes that the reaction of CH_3–S–CoM and $Ni^{I}F_{430}$ gives a $Ni^{II}F_{430}$thiolate and a free CH_3• radical. The latter radical is immediately quenched by H-transfer from HS–CoB [118,119].

A first strong indication for mechanism *A* follows from the reaction of MCR with the irreversible inhibitor 3-bromopropane sulphonate (BPS) [120]. Q-band Davies-ENDOR and HYSCORE in combination with ^{13}C labeling allowed for the identification of the bond formed between the nickel atom and the C_γ atom of the propane sulphonate residue. DFT computations of the EPR parameters of an [alkyl-$Ni^{III}F_{430}^{+}$] model, agreed very well with the observed experimental data. Similarly, ENDOR techniques played a crucial role in identifying the formation of [CH_3–$Ni^{III}F_{430}^{+}$] species by reaction of MCR with $BrCH_3$ [121] and ICH_3 [122].

The active form of MCR is referred to as the MCR_{red1} state. It is formed when the gas mixture used for cell growth (80% H_2/20% CO_2) is made more reducing (100% H_2). Different sub-forms have been distinguished: MCR_{red1a} which is the red1 form in the absence of other compounds (Fig. 11b), MCR_{red1c} which is the red1 molecule with coenzyme M (H–S–CoM) present and MCR_{red1m} indicating the red1 in the presence of methyl-coenzyme M [123–126]. The CW-EPR spectra of MCR_{red1a} and the isolated $Ni^{I}F_{430}$ complex are very similar and bear all the characteristics of a Ni^{I} complex with the unpaired electron residing in the $d_{x^2-y^2}$ orbital. The principal *g* values of the three red1 subforms are slightly different, indicating a clear influence and possible binding of the (methyl-)coenzyme M molecules ([125,126], Table 2).

When the cells are grown in an 80% N_2/20% CO_2 mixture, *i.e.* under more oxidizing conditions, MCR is found in the ox1 state. It can be converted into the red1 state by incubation with Ti(III) citrate [127]. There is a pronounced difference between the principal *g* values determined by W-band CW-EPR for the ox1 state and the ones reported for the red1 forms (Table 2, Ref. [128]). A multi-frequency EPR, ENDOR and HYSCORE study in combination with ^{2}H, ^{61}Ni and ^{33}S labeling revealed that the MCR_{ox1} metal centre can be described as a Ni^{III}-thiolate (Fig. 11c) in resonance with a thiyl radical/high-spin Ni^{II} complex [128]. The former structure is the dominant one.

MCR_{red1a} can be converted into a red2 form by addition of coenzyme M (to form MCR_{red1c}) and subsequent addition of HS–CoB. High-field EPR revealed that two structures are formed: MCR_{red2a} characterized by an axial EPR spectrum and MCR_{red2r} with a typical rhombic EPR spectrum [129]. In a very detailed multi-frequency Davies-ENDOR and HYSCORE study, combined with extensive DFT modeling, Harmer and co-workers revealed that the MCR_{red2a} form can be described as an intermediate between a Ni^{III}-hydride and an agostic interaction of the CoM–S–H hydrogen with Ni^{I} [130]. The hydride formation is indicated by the detection of a large proton hyperfine coupling ([−43 −42 −5] MHz) and its discovery is extremely important from a mechanistic point of view because of the known ability of hydrides to activate methane [132]. This study presents a nice illustration of the power of modern-day EPR, whereby the latest state-of-the-art EPR spectroscopy, such as REFINE (relaxation time filtered) HYSCORE [131], is used to gain information that is not accessible by other means.

Although no satisfying theoretical structural model can at the moment be presented for MCR_{red2r} that agrees with the experimental EPR findings, different constraints can be proposed based on the extensive multi-frequency EPR and ENDOR studies [130,133,134].

The thiol sulphur of coenzyme M is coordinated to the nickel, an exchangeable proton is close to the nickel on a Ni–H vector at an angle of ∼60° or ∼120° from the Ni–S bond, a displacement of the pyrrole A of the F_{430} macrocycle is occurring inducing a large anisotropic distribution of the spin density, and the carboxamide group of $Gln^{\alpha'147}$ is no longer coordinating the nickel atom from the distal side.

6. Conclusions

To obtain a complete structural characterization of any paramagnetic species, it is first necessary to establish the chemical identity, geometric structure and electronic structure of the system. As we have shown, this information can be extracted from a combination of modern advanced EPR techniques. Owing to the high sensitivity of these methods, and due to the fact that the desired spectroscopic information can be obtained in frozen solutions (without the need for single crystals), the investigation of homogeneous asymmetric complexes incorporating transition-metal ions will benefit enormously from state-of-the-art EPR techniques. It is clear that the design and synthesis of chiral ligands that can coordinate transition-metal ions, and, hence, induce high stereoselectivities for organic transformations, constitutes an important area of modern coordination chemistry. Of paramount importance in this development, is the need to better understand the mechanisms and structure–function relations of the asymmetric reactions in solution. Since the family of EPR techniques, including high-field EPR, ESEEM, ENDOR and ELDOR-detected NMR, provide information, not only on the localized transition-metal ions, but also on the remote hyperfine interactions with ligand and substrate/reactant/product nuclei, an unrivaled structural model of the active site can be achieved. The power of EPR is even increased by combining the experimental studies with DFT computations. With this promising potential, EPR will hopefully be exploited more in the future for the understanding of asymmetric reaction mechanisms.

Acknowledgments

This work was supported by the Fund of Scientific Research-Flanders (FWO) (Project G.0312.05N to S.V.D.). D.M.M. and I.A.F. acknowledge the support of EPSRC (EP/E030122). I.C.G. acknowledges the financial support provided by the Spanish Foundation for Science and Technology (FECYT) in collaboration with the State secretariat of Universities and Research (Ministry of Science & Education).

References

[1] C.-M. Che, J.-S. Huang, Coord. Chem. Rev. 242 (2003) 97.
[2] E.N. Jacobsen, A. Pfaltz, H. Yamamoto (Eds.), Comprehensive Asymmetric Catalysis, Springer, New York, 1999.
[3] M. Movassaghi, E.N. Jacobsen, Science 298 (2002) 1904.
[4] M.S. Taylor, E.N. Jacobsen, Angew. Chem. Int. Ed. 45 (2006) 1520.
[5] M. Heitbaum, F. Glorius, I. Escher, Angew. Chem. Int. Ed. 45 (2006) 4732.
[6] T.P. Yoon, E.N. Jacobsen, Science 299 (2003) 1691.
[7] J.M. Fraile, J.I. Garcia, G. Jimenez-Oses, J.A. Mayoral, M. Roldan, Organometalics 27 (2008) 2246.
[8] D. Di Tommaso, S.A. French, A. Zanotti-Gerosa, F. Hancock, E.J. Palin, C.R.A. Catlow, Inorg. Chem. 47 (2008) 2674.
[9] Y. Ihori, Y. Yamashita, H. Ishitani, S. Kobayashi, J. Am. Chem. Soc. 44 (2005) 15528.
[10] P. Brandt, M.J. Södergren, P. Gandersson, P.-O. Norrby, J. Am. Chem. Soc. 112 (2000) 8013.
[11] P. Brandt, P.-O. Norrby, A.M. Daly, D.G. Gilheany, Chem. Eur. J. 8 (2002) 4299.
[12] E. Carter, D.M. Murphy, Spec. Period. Rep., Spectrosc. Proper. Inorg. Organometal. Compd. 40, in press.
[13] J.A. Weil, J.R. Bolton, J.E. Wertz, Electron Paramagnetic Resonance, Wiley, New York, 1994.
[14] D. Goldfarb, Phys. Chem. Chem. Phys. 8 (2006) 2325.
[15] D. Goldfarb, D. Arieli, Annu. Rev. Phys. Chem. 33 (2004) 441.
[16] T. Prisner, M. Rohrer, F. MacMillan, Annu. Rev. Phys. Chem. 52 (2001) 279.
[17] J. Krzystek, A. Ozarowski, J. Telser, Coord. Chem. Rev. 150 (2006) 2308.
[18] J.H. Freed, Annu. Rev. Phys. Chem. 51 (2000) 655.
[19] K. Möbius, A. Savitsky, A. Schnegg, M. Plato, M. Fuchs, Phys. Chem. Chem. Phys. 7 (2005) 19.
[20] A. Schweiger, G. Jeschke, Principles of Pulse Electron Paramagnetic Resonance, University Press Oxford, Oxford, 2001.
[21] W. Lubitz, E. Reijerse, M. van Gastel, Chem. Rev. 107 (2007) 4331.
[22] K. Kristoffer, P.P. Schmidt, B. Katterle, K.R. Strand, A.E. Palmer, S.-K. Lee, E.I. Solomon, A. Gräslund, A.-L. Barra, J. Biol. Inorg. Chem. 8 (2003) 235.
[23] M. Bennati, T. Prisner, Rep. Prog. Phys. 68 (2005) 411.
[24] S. Van Doorslaer, E. Vinck, Phys. Chem. Chem. Phys. 9 (2007) 4620.
[25] J.R. Pilbrow, Transition Ion Electron Paramagnetic Resonance, Clarendon, Oxford, 1990.
[26] J. Keeler, Understanding NMR Spectroscopy, J. Wiley & Sons Ltd., West Sussex, 2005.
[27] P. Höfer, A. Grupp, H. Nebenführ, M. Mehring, Chem. Phys. Lett. 132 (1986) 279.
[28] G. Jeschke, R. Rakhmatullin, A. Schweiger, J. Magn. Reson. 131 (1998) 261.
[29] L. Liesum, A. Schweiger, J. Chem. Phys. 114 (2001) 9478.
[30] G. Feher, Phys. Rev. 103 (1956) 834.
[31] H. Kurreck, B. Kirste, W. Lubitz, Electron Nuclear Double Resonance Spectroscopy of Radicals in Solution, VCH Publishers, New York, 1988.
[32] C. Gemperle, A. Schweiger, Chem. Rev. 91 (1991) 1481.
[33] I.A. Gromov, J. Harmer, Appl. Magn. Reson. 31 (2007) 627.
[34] E.R. Davies, Phys. Lett. A47 (1974) 1.
[35] W.B. Mims, Proc. R. Soc. 283 (1965) 452.
[36] G. Jeschke, A. Schweiger, Chem. Phys. Lett. 246 (1995) 431.
[37] H. Thomann, M. Bernardo, Methods Enzymol. 227 (1993) 118.
[38] P. Schosseler, Th. Wacker, A. Schweiger, Chem. Phys. Lett. 224 (1994) 319.
[39] M. Fittipaldi, I. García-Rubio, F. Trandafir, I. Gromov, A. Schweiger, A. Bouwen, S. Van Doorslaer, J. Phys. Chem. B 112 (2008) 3859.
[40] A. Potapov, B. Epel, D. Goldfarb, J. Chem. Phys. 128 (2008) 052320.
[41] G.C. Hurst, T.A. Henderson, R.W. Kreilick, J. Am. Chem. Soc. 107 (1985) 7294.
[42] S. Van Doorslaer, Spec. Period. Rep., Electron Paramagn. Reson. 21 (2008) 162.
[43] M. Kaupp, M. Bühl, V.G. Malkin (Eds.), Calculation of NMR and EPR Parameters, Wiley–VCH, Weinheim, 2004.
[44] F. Neese, E.I. Solomon, in: J.S. Miller, M. Drillon (Eds.), Magnetism: Molecules to Materials, vol. IV, Wiley–VCH, Weinheim, 2003, p. 345.
[45] M. van Gastel, C. Fichtner, F. Neese, W. Lubitz, Biochem. Soc. Trans. 33 (2005) 7.
[46] D. Baute, D. Arieli, F. Neese, H. Zimmermann, B.M. Weckhuysen, D. Goldfarb, J. Am. Chem. Soc. 126 (2004) 11733.
[47] F. Neese, Spec. Period. Rep., Electron Spin Reson. 20 (2007) 73.
[48] P.H. Rieger, Electron Spin Resonance; Analysis and Interpretation, RSC Publishing, 2007.
[49] F.E. Mabbs, D. Collison, Studies in Inorganic Chemistry 16: Electron Paramagnetic Resonance of d-Transition Metal Compounds, Elsevier, 1992.
[50] F.E. Mabbs, Chem. Soc. Rev. (1993) 313.
[51] S. Deblon, L. Liesum, J. Harmer, H. Schönberg, A. Schweiger, H. Grützmacher, Chem. Eur. J. 8 (2002) 601.
[52] F. Breher, C. Böhler, G. Frison, J. Harmer, L. Liesum, A. Schweiger, H. Grützmacher, Chem. Eur. J. 9 (2003) 3859.
[53] P. Maire, A. Sreekanth, T. Büttner, J. Harmer, I. Gromov, H. Rüegger, F. Breher, A. Schweiger, H. Grützmacher, Angew. Chem. Int. Ed. 45 (2006) 3265.
[54] J.L. Esker, M. Newcomb, Adv. Heterocycl. Chem. 58 (1993) 1.
[55] J. Stubbe, W.A. van der Donk, Chem. Rev. 98 (1998) 705.
[56] T. Büttner, J. Geier, G. Frison, J. Harmer, C. Calle, A. Schweiger, H. Schönberg, H. Grützmacher, Science 307 (2005) 235.
[57] L.R. Milgrom, The Colours of Life: An Introduction to the Chemistry of Porphyrins and Related Compounds, Oxford University Press, Oxford, 1997.
[58] N.B. McKeown, Phthalocyanine Materials: Synthesis, Structure and Function, Cambridge University Press, London, 1998.
[59] B. Kräutler, D. Arigoni, B.T. Golding (Eds.), Vitamin B_{12} and B_{12} Proteins, Wiley–VCH, Weinheim, 1998.
[60] G. Simonneaux, P. Le Maux, Y. Ferrand, J. Rault-Berthelot, Coord. Chem. Rev. 250 (2006) 2212.
[61] T.D. Smith, J.R. Pilbrow, Coord. Chem. Rev. 39 (1981) 295.
[62] S. Van Doorslaer, R. Bachmann, A. Schweiger, J. Phys. Chem. A 103 (1999) 5446.
[63] S. Van Doorslaer, A. Schweiger, J. Phys. Chem. B 104 (2000) 2919.
[64] S. Van Doorslaer, A. Schweiger, B. Kräutler, J. Phys. Chem. B 105 (2001) 7554.
[65] S. Van Doorslaer, A. Schweiger, Phys. Chem. Chem. Phys. 3 (2001) 159.
[66] J. Harmer, S. Van Doorslaer, I. Gromov, M. Broering, G. Jeschke, A. Schweiger, J. Phys. Chem. B 106 (2002) 2801.
[67] S. Van Doorslaer, G. Jeschke, B. Epel, D. Goldfarb, R.-A. Eichel, B. Kräutler, A. Schweiger, J. Am. Chem. Soc. 125 (2003) 5915.
[68] C. Finazzo, S. Van Doorslaer, A. Schweiger, J. Porph. Phthal. 7 (2003) 89.
[69] C. Finazzo, C. Calle, S. Stoll, S. Van Doorslaer, A. Schweiger, Phys. Chem. Chem. Phys. 8 (2006) 1942.
[70] E. Vinck, S. Van Doorslaer, Phys. Chem. Chem. Phys. 6 (2004) 5324.
[71] D. Lexa, J.M. Saveant, Acc. Chem. Res. 16 (1983) 235.
[72] M. Giorgetti, I. Ascone, M. Berrettoni, P. Conti, S. Zamponi, R. Marassi, J. Biol. Inorg. Chem. 5 (2000) 156.
[73] E.M. Scheuring, W. Clavin, M.D. Wirt, L.M. Miller, Y.L. Fischetti, N. Mahoney, A. Xie, J. Wu, M.R. Chance, J. Phys. Chem. 100 (1996) 3344.
[74] A. Togni, G. Rist, G. Rihs, A. Schweiger, J. Am. Chem. Soc. 115 (1993) 1908.

[75] A. Togni, Organometallics 9 (1990) 3106.
[76] N.S. Venkataramanan, G. Kupuraj, S. Rajagopal, Coord. Chem. Rev. 249 (2005) 1249.
[77] W. Zhang, J.L. Loebach, S.R. Wilson, E.N. Jacobsen, J. Am. Chem. Soc. 112 (1990) 2801.
[78] R. Irie, K. Noda, Y. Ito, N. Matsumoto, T. Katsuki, Tetrahedron Lett. 31 (1990) 7345.
[79] T. Katsuki, Coord. Chem. Rev. 140 (1995) 189.
[80] L. Canali, D.C. Sherrington, Chem. Soc. Rev. 28 (1999) 85.
[81] K. Srinivasan, P. Michaud, J.K. Kochi, J. Am. Chem. Soc. 108 (1986) 2309.
[82] K.P. Bryliakov, D.E. Babushkin, E.P. Talsi, Mendeleev Commun. (1999) 29.
[83] K.P. Bryliakov, D.E. Babushkin, E.P. Talsi, J. Mol. Catal. A 158 (2000) 19.
[84] K.P. Bryliakov, I.V. Khavrutskii, E.P. Talsi, O.A. Kholdeeva, React. Kinet. Catal. Lett. 71 (2000) 183.
[85] K.P. Bryliakov, O.A. Kholdeeva, M.P. Vanina, E.P. Talsi, J. Mol. Catal. A 178 (2002) 47.
[86] K.A. Campbell, M.R. Lashley, J.K. Wyatt, M.H. Nantz, R.D. Britt, J. Am. Chem. Soc. 123 (2001) 5710.
[87] R.D. Britt, J.M. Peolquin, K.A. Campbell, Annu. Rev. Biophys. Biomol. Struct. 29 (2000) 463.
[88] W.-Y. Hsieh, V.L. Pecoraro, Inorg. Chim. Acta 341 (2002) 113.
[89] I. García-Rubio, M. Fittipaldi, F. Trandafir, S. Van Doorslaer, Inorg. Chem. 47 (2008) 11294.
[90] I.A. Fallis, D.M. Murphy, D.J. Willock, R.J. Tucker, R.D. Farley, R. Jenkins, R.R. Strevens, J. Am. Chem. Soc. 126 (2004) 15660.
[91] D.M. Murphy, I.A. Fallis, D.J. Willock, J. Landon, E. Carter, E. Vinck, Angew. Chem. Int. Ed. 47 (2008) 1414.
[92] C. Bolm, Coord. Chem. Rev. 237 (2003) 245.
[93] E. Tsuchida, K. Oyaizu, Coord. Chem. Rev. 37 (2003) 213.
[94] L.P.C. Nielsen, C.P. Stevenson, D.G. Blackmond, E.N. Jacobsen, J. Am. Chem. Soc. 126 (2004) 1360.
[95] E. Vinck, S. Van Doorslaer, D.M. Murphy, I.A. Fallis, Chem. Phys. Lett. 464 (2008) 31.
[96] M. Tokunaga, J.F. Larrow, F. Kakiuchi, E.N. Jacobsen, Science 277 (1997) 936.
[97] K.P. Bryliakov, M.V. Lobanova, E.P. Talsi, J. Chem. Soc. Dalton Trans. (2002) 2263.
[98] K.P. Bryliakov, E.P. Talsi, Inorg. Chem. 42 (2003) 7258.
[99] C. Bolm, O. Simic, J. Am. Chem. Soc. 123 (2001) 3830.
[100] C. Bolm, M. Martin, G. Gescheidt, C. Palivan, D. Neshchadin, H. Bertagnolli, M. Feth, A. Schweiger, G. Mitrikas, J. Harmer, J. Am. Chem. Soc. 125 (2003) 6222.
[101] C. Bolm, M. Martin, G. Gescheidt, C. Palivan, T. Stanoeva, H. Bertagnolli, M. Feth, A. Schweiger, G. Mitrikas, J. Harmer, Chem. Eur. J. 13 (2007) 1842.
[102] J.S. Johnson, D.A. Evans, Accs. Chem. Res. 33 (2000) 325.
[103] G. Helmchen, A. Pfaltz, Acc. Chem. Res. 33 (2000) 336.
[104] J.M. Fraile, J.I. Garcia, J.A. Mayoral, Coord. Chem. Rev. 252 (2008) 624.
[105] D. Rechavi, M. Lemaire, Chem. Rev. 102 (2002) 3467.
[106] Y. Traa, D.M. Murphy, R.D. Farley, G.J. Hutchings, Phys. Chem. Chem. Phys. 3 (2001) 1073.
[107] Y. Deligiannakis, M. Louloudi, N. Hadjiliadis, Coord. Chem. Rev. 204 (2000) 1.
[108] M. Ubbink, J.a.R. Worrall, G.W. Canters, E.J.J. Groenen, M. Huber, Annu. Rev. Biophys. Biomol. Struct. 31 (2002) 393.
[109] T.S. Smith, R. LoBrutto, V.L. Pecoraro, Coord. Chem. Rev. 228 (2002) 1.
[110] R.K. Thauer, Microbiology 144 (1998) 2377.
[111] U. Ermler, W. Grabase, S. Shima, M. Goubeaud, R.K. Thauer, Science 278 (1997) 1457.
[112] S. Shima, M. Goubeaud, D. Vinzenz, R.K. Thauer, U. Ermler, J. Mol. Biol. 303 (2000) 329.
[113] W. Grabarse, F. Mahlert, S. Shima, E.C. Duin, M. Goubeaud, S. Sima, R.K. Thauer, V. Lamzin, U. Ermler, J. Mol. Biol. 309 (2001) 315.
[114] B. Jaun, Helv. Chim. Acta 73 (1990) 2209.
[115] W.L. Ellefson, W.B. Whitman, R.S. Wolfe, Proc. Natl. Acad. Sci. U.S.A. 79 (1982) 3707.
[116] Y.-C. Horng, D.F. Becker, S.W. Ragsdale, Biochemistry 40 (2001) 12875.
[117] M. Groenrich, E.C. Duin, F. Mahlert, R.K. Thauer, J. Biol. Inorg. Chem. 10 (2005) 333.
[118] V. Pelmenshikov, P.E.M. Siegbahn, J. Biol. Inorg. Chem. 8 (2003) 653.
[119] V. Pelmenshikov, M.R.A. Blomberg, P.E.M. Siegbahn, R.H. Crabtree, J. Am. Chem. Soc. 124 (2002) 4039.
[120] D. Hinderberger, R.P. Piskorski, M. Groenrich, R.K. Thauer, A. Schweiger, J. Harmer, B. Jaun, Angew. Chem. Int. Ed. 45 (2006) 3602.
[121] N. Yang, M. Reiher, M. Wang, J. Harmer, E.C. Duin, J. Am. Chem. Soc. 129 (2007) 11028.
[122] M. Dey, J. Telser, R.C. Kunz, N.S. Lees, S.W. Ragsdale, B.M. Hoffman, J. Am. Chem. Soc. 129 (2007) 11030.
[123] J. Telser, Y.-C. Fann, M.W. Renner, J. Fajer, S. Wang, H. Zhang, R.A. Scott, B.M. Hoffman, J. Am. Chem. Soc. 119 (1997) 733.
[124] J. Telser, Y.C. Horng, D.F. Becker, B.M. Hoffman, S.W. Ragsdale, J. Am. Chem. Soc. 122 (2000) 182.
[125] F. Mahlert, W. Grabarse, J. Kahnt, R.K. Thauer, E.C. Duin, J. Biol. Inorg. Chem. 7 (2002) 101.
[126] E.C. Duin, L. Signor, R. Piskorski, F. Mahlert, M.D. Clay, M. Goenrich, R.K. Thauer, B. Jaun, M.K. Johnson, J. Biol. Inorg. Chem. 9 (2004) 563.
[127] M. Goubeaud, G. Schreiner, R.K. Thauer, Eur. J. Biochem. 243 (1997) 110.
[128] J. Harmer, C. Finazzo, R. Piskorski, C. Bauer, B. Jaun, E.C. Duin, M. Goenrich, R.K. Thauer, S. Van Doorslaer, A. Schweiger, J. Am. Chem. Soc. 127 (2005) 17744.
[129] D.I. Kern, M. Groenich, B. Jaun, R.K. Thauer, J. Harmer, D. Hinderberger, J. Biol. Inorg. Chem. 12 (2007) 1097.
[130] J. Harmer, C. Finazzo, R. Piskorski, S. Ebner, E.C. Duin, M. Goenrich, R.K. Thauer, M. Reiher, A. Schweiger, D. Hinderberger, B. Jaun, J. Am. Chem. Soc. 130 (2008) 10907.
[131] T. Maly, T.F. Prisner, J. Magn. Reson. 170 (2004) 88.
[132] M. Slangen, H. Schwarz, Angew. Chem. Int. Ed. 46 (2007) 5614.
[133] C. Finazzo, J. Harmer, B. Jaun, E.C. Duin, F. Mahlert, R.K. Thauer, S. Van Doorslaer, A. Schweiger, J. Biol. Inorg. Chem. 8 (2003) 586.
[134] C. Finazzo, J. Harmer, C. Bauer, B. Jaun, E.C. Duin, F. Mahlert, M. Goenrich, R.K. Thauer, S. Van Doorslaer, A. Schweiger, J. Am. Chem. Soc. 125 (2003) 4988.